



# Large-eddy simulation of an atmospheric bore and associated gravity wave effects on wind farm performance in the southern Great Plains

Adam S. Wise<sup>1,2</sup>, Robert S. Arthur<sup>2</sup>, Aliza Abraham<sup>3</sup>, Sonia Wharton<sup>2</sup>, Raghavendra Krishnamurthy<sup>4</sup>, Rob Newsom<sup>4</sup>, Brian Hirth<sup>5</sup>, John Schroeder<sup>6</sup>, Patrick Moriarty<sup>3</sup>, and Fotini K. Chow<sup>1</sup>

<sup>1</sup>Department of Civil and Environmental Engineering, University of California, Berkeley, California, USA

<sup>2</sup>Lawrence Livermore National Laboratory, Livermore, California, USA

<sup>3</sup>National Renewable Energy Laboratory, Golden, Colorado, USA

<sup>4</sup>Pacific Northwest National Laboratory, Richland, Washington, USA

<sup>5</sup>National Wind Institute, Texas Tech University, Lubbock, Texas, USA

<sup>6</sup>Department of Geosciences, Texas Tech University, Lubbock, Texas, USA

**Correspondence:** Adam S. Wise (adamwise@berkeley.edu)

Received: 5 July 2024 – Discussion started: 26 August 2024

Revised: 24 January 2025 – Accepted: 2 March 2025 – Published: 2 June 2025

**Abstract.** Gravity waves are a common occurrence in the atmosphere, with a variety of generation mechanisms. Their impact on wind farms has only recently gained attention, with most studies focused on wind farm-induced gravity waves. In this study, the interaction between a wind farm and gravity waves generated by an atmospheric bore event is assessed using multiscale large-eddy simulations. The atmospheric bore is created by a thunderstorm downdraft from a nocturnal mesoscale convective system (MCS). The associated gravity waves impact the wind resource and power production at a nearby wind farm during the American Wake Experiment (AWAKEN) in the US southern Great Plains. A two-domain nested setup ( $\Delta x = 300$  and 20 m) is used in the Weather Research and Forecasting (WRF) model, forced with data from the High-Resolution Rapid Refresh model, to capture both the formation of the bore and its interaction with individual wind turbines. The MCS is resolved on the large outer domain, where the structure of the bore and the associated gravity waves are found to be especially sensitive to parameterized microphysics processes. On the finer inner domain, gravity wave interactions with individual wind turbines are resolved; wake dynamics are captured using a generalized actuator disk parameterization in WRF. The gravity waves are found to have a strong effect on the atmosphere above the wind farm; however, the effect of the waves is more nuanced closer to the surface where there is additional turbulence, both ambient and wake-generated. Notably, the gravity waves modulate the mesoscale environment by weakening and dissipating the preexisting low-level jet, which reduces hub-height wind speed and hence the simulated power output, which is confirmed by the observed supervisory control and data acquisition (SCADA) power data. Additionally, the gravity waves induce local wind direction variations correlated with fluctuations in pressure, which lead to fluctuations in the simulated power output as various turbines within the farm are subjected to waking from nearby turbines.

## 1 Introduction

The United States (US) southern Great Plains, and more specifically, Oklahoma, is a region with significant wind turbine and wind farm development. Oklahoma currently has nearly 12 GW of installed wind capacity, and the state has recently generated over 44 % of its electricity demand from wind power, enough to power 3.3 million homes (U.S. Energy Information Administration, 2023). The region has abundant wind energy resources and is an area that will see continued wind farm development; it is critical to study atmosphere–wind farm interactions in this region further. In the southern Great Plains, there are a number of relevant atmospheric science phenomena for which the effect on wind turbines and wind farms is not well understood. One such phenomenon, which is of particular interest to the wind energy community as part of the ongoing American Wake Experiment (AWAKEN) (Moriarty et al., 2020; Debnath et al., 2022; Moriarty et al., 2024), is intermittent or wavy turbulence.

In general, wavy turbulence in the atmosphere can be either shear-driven or buoyancy-driven. For shear-driven waves, competing shear- and buoyancy-driven effects result in an instability (Stull, 1988), thus inducing waves. Shear-driven waves commonly occur beneath low-level jets (LLJs), which exhibit a large amount of shear, and are dependent on local atmospheric conditions (Newsom and Banta, 2003). The occurrence of shear-driven waves in the US Great Plains can depend on local topography, such as shallow river valleys, or land-use variability that affects wind shear profiles via changes in surface roughness. Buoyancy-driven waves, also known as gravity waves, generally occur due to perturbations in a stably stratified atmosphere (Stull, 1988). Gravity wave generation mechanisms include frontal systems, thunderstorms, and mountains (Rottman and Simpson, 1989; Ralph et al., 1999; Stull, 1988; Geerts et al., 2017) or even the wind farms themselves (Allaerts and Meyers, 2018; Lanzilao and Meyers, 2022; Stipa et al., 2024). Waves generated by mountains and wind farms are typically standing waves, while waves generated by frontal systems and thunderstorms propagate with a wave speed that depends on atmospheric conditions.

In this study, we focus on gravity waves associated with atmospheric bore events, which are commonly observed in the US Great Plains. Bores are often generated by a nocturnal mesoscale convective system (MCS) (Haghi et al., 2019; Feng et al., 2019). In this case, a cold air pool created by the thunderstorm downdraft spreads radially as a density current resulting in a bore (Rottman and Simpson, 1989; Toms et al., 2017; Johnson et al., 2018; Haghi et al., 2019; Haghi and Durran, 2021) (although, note that density currents can also be generated by distant cold fronts, atmospheric mesoscale disturbances, or rapid surface cooling (Simpson, 1997; Sun et al., 2002; Lundquist, 2003)). Bores result in a temporary increase in the depth of the sta-

ble boundary layer (SBL), along with wavy oscillations and a shift in wind speed and wind direction associated with the propagation of the bore (Knupp, 2006).

Bore events were a major focus of the Plains Elevated Convection at Night (PECAN) field campaign, which took place during June and July 2015 (Geerts et al., 2017). PECAN set out to study nocturnal deep convection using a number of instruments, including mobile Doppler lidars, radars, atmospheric emitted-radiance interferometers, radiosondes, and aircraft observations. Six intensive observational periods (IOPs) and two unofficial field operations were dedicated to bores, although bores were also observed during IOPs focused on other processes (Geerts et al., 2017; Weckwerth et al., 2019; Weckwerth and Romatschke, 2019).

In addition to the data gathered to characterize bores, forecasting and modeling of bores was also a critical component of the field campaign. Johnson et al. (2018) and Johnson and Wang (2019) conducted a number of Weather Research and Forecasting (WRF) model evaluations for predicting bores during PECAN. In their studies, they initialized simulations using the grid-point statistical-interpolation-based ensemble Kalman filter technique, where both in situ and convective-scale radar data are assimilated (Johnson and Wang, 2017; Johnson et al., 2017). They found that the bore structure is especially sensitive to microphysics parameterizations, as microphysical low-level cooling within convection determines the strength of the cold pool. Other studies focused on deep convection have also found large modeling sensitivities to microphysics schemes (Pandey et al., 2023; Han et al., 2019). Johnson and Wang (2019) assessed the sensitivity of model predictions to the horizontal and vertical grid spacing, as well as the turbulence closure. They found that 250 m grid spacing offered improved results compared to 1 km grid spacing, with further improvement when using large-eddy simulation (LES). Additionally, enhanced low-level vertical resolution improved simulation results. For an additional discussion on nocturnal convection initiation and the forecastability of MCSs and bores in general, see Weckwerth and Romatschke (2019) and Weckwerth et al. (2019).

In the present work, LES is used to examine how an atmospheric bore and its associated gravity waves affect wind farm performance. LES explicitly solves for the most energetic turbulent eddies in the atmospheric boundary layer (ABL) while parameterizing the effects of the smaller turbulent length scales on the resolved-scale flow. LES is especially well suited to capture transient and dynamic turbulent flow structures, such as bores, which are important features of the ABL that interact with wind farms. We use a nested multiscale framework in the WRF model v4.4 (Skamarock et al., 2021), which allows us to explicitly resolve the convective scales that generate the bore. The impact of the bore on the wind farm is simultaneously parameterized using a generalized actuator disk (GAD) to resolve the finer-scale turbulence associated with wind turbine wakes (Mirocha et al., 2014; Aitken et al., 2014). The WRF-LES framework along

with the GAD parameterization is hereinafter denoted as WRF-LES-GAD to describe the model in its entirety.

The goals of this study are to (1) design a multiscale framework to analyze bore–wind farm interactions, (2) analyze the sensitivity of the bore structure to modeling parameters, and (3) analyze how an intermittent turbulence event such as from a bore can modulate wind farm power production. To accomplish these goals, we use WRF-LES-GAD to model the King Plains wind farm in Oklahoma, which is a major focus of the AWAKEN field campaign (described in more detail in Sect. 2). The WRF-LES-GAD modeling setup is described in detail in Sects. 3 and 4, focusing on the microphysics schemes and LES turbulence closures which are known to affect model performance. Observations of the atmospheric bore and its characteristics at various times are compared with modeling results in Sect. 5. Lastly, the effect of the gravity waves on the simulated wind farm’s power production is also quantified in Sect. 5 by analyzing time periods before, during, and after the gravity waves pass the Kings Plains wind farm.

## 2 Case study

### 2.1 Overview of the AWAKEN field campaign

The American Wake Experiment (AWAKEN) field campaign began in September 2022 with a scheduled end date of September 2025. AWAKEN is centered around five wind farms in northern Oklahoma near the town of Enid. While the AWAKEN domain covers a number of wind farms, the bulk of the instrumentation is located in the eastern half of the King Plains wind farm, which includes 50 wind turbines (see Fig. 1). The aim of the field campaign is to better understand wind farm–atmosphere interaction, and as part of AWAKEN, there are seven testable hypotheses (Moriarty et al., 2024). The focus of this study is on the hypothesis that intermittent turbulent bursting events related to Kelvin–Helmholtz instability, gravity waves, and bores lead to fluctuations in wind farm power production and structural loading of wind turbines. Specifically, this study is concerned with the effect of bores and associated gravity waves on wind farm power production.

The dominant wind direction in the region is southerly (Krishnamurthy et al., 2021; Debnath et al., 2023), which determined the design of a north–south instrument transect through the King Plains wind farm. In this study, we focus on data collected with remote sensing Doppler lidars at Site A1 (see Fig. 4). A scanning Doppler lidar (Halo Streamline XR+) deployed by Atmospheric Radiation Measurement (ARM) (Newsom and Krishnamurthy, 2022) ran composite scans for 20 min of six-beam profiling (Sathe et al., 2015) and 10 min of vertical stares. The scanning Doppler lidar has a range gate of 30 m and measured from 90 m to the top of the ABL with a temporal resolution of approximately 6 s per wind profile. The six-

beam profiles are used for comparison in this study, with a least squares fit to the radial velocity measurement (Krishnamurthy et al., 2025). At Site A1, an additional short-range vertical profiling Doppler lidar was deployed by Lawrence Livermore National Laboratory (LLNL) to focus on the wind turbine rotor layer (40 to 240 m). This higher-resolution lidar at A1 was a WindCube v2, which has a scan frequency of approximately 4 s.

This study also includes measurements generated by two X-band radars from Texas Tech University (TTU) (Hirth et al., 2017; Debnath et al., 2022; Hirth et al., 2024). These radars provide wind measurements over a large portion of the study region (see Fig. 1), performing 145° horizontal scans over a vertical range of 2°, resulting in observations over a three-dimensional volume roughly every 2 min. Dual-Doppler reconstruction is used to obtain the horizontal velocity vector field from the radial wind speeds recorded by the radars. In their near range, the radars provide observations with a grid spacing as fine as 25 m. However, the eastern half of the King Plains wind farm, which is the focus of this study, is on the edge of the maximum radar range, where the radar measurements are interpolated to a grid spacing of 50 m. Additionally, it is worth noting that there are areas without returns within the rotor-swept area due to the lower elevation of the eastern half of the King Plains wind farm as the radar beam is blocked by terrain variations. There is also the impact of the Earth’s curvature where at ranges of 20, 25, and 30 km curvature accounts for shifts in vertical height of 49, 70, and 96 m, respectively.

There are surface-based meteorological (met) stations scattered throughout the AWAKEN domain, which are used to characterize atmospheric surface layer stability. At Site A1, an eddy correlation (ECOR) flux measurement system was deployed from April until September 2024 (Cook, 2018). The ECOR system includes a sonic anemometer mounted 3 m above ground level (a.g.l.), measuring three-dimensional wind at 10 Hz. The data are post-processed in near-real time into 30 min fluxes. Fast-response wind and temperature measurements from the sonic anemometer are used to derive the Obukhov length.

Lastly, high-frequency power output data at 1 Hz from the supervisory control and data acquisition (SCADA) system are also available for the King Plains wind farm. Simulated and observed power are qualitatively compared in Sect. 5.4 to demonstrate the dynamic effects of the bore and associated gravity waves on power output. The observed power data are normalized at the request of the wind farm operator.

### 2.2 Case study description

The phenomenon of interest in this work is an atmospheric bore with associated gravity waves. The historical weather radar imagery indicates that the weather consisted of localized precipitation on 6 June 2023. Figure 2 shows the weather radar reflectivity from the NEXRAD (Next Gener-

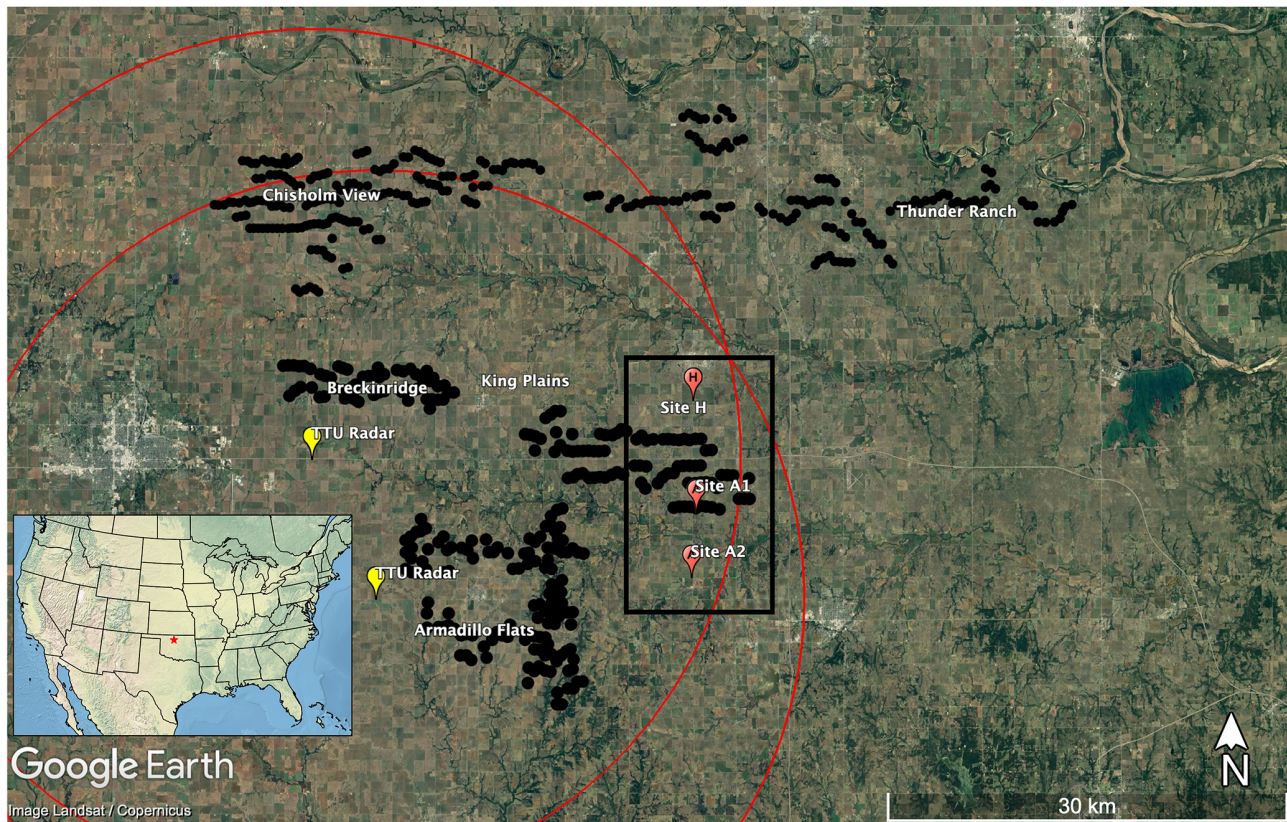


**Figure 1.** AWAKEN region with instrumented sites relevant to this site and black dots representing individual turbines. The red star on the inset map of the continental USA is the location of the AWAKEN region within the state of Oklahoma. The X-band radar ranges are highlighted with red circles. The area representing WRF domain d02 is outlined in black and covers the eastern half of the King Plains wind farm (see Fig. 4). © Google Earth.

ation Weather Radar) weather surveillance radar 88D (WSR-88D) system at the Oklahoma City radar site (KTLX), operated by the US National Weather Service. The radar images in Fig. 2 are from 03:30 to 05:00 UTC (22:30 to 00:00 LT, local time) in 30 min intervals. However, the radar returns have a roughly 4 min temporal resolution, and an animation of the event is available (see the “Video supplement” section for details). Localized precipitation caused by a cluster of thunderstorms is evident as increased reflectivity in Fig. 2. These storms form an organized nocturnal mesoscale convective system (MCS). At 03:30 UTC, the cold pool outflow from the MCS is evident as a fine line to the north and west of the MCS center. Similar outflow boundaries are commonly observed along with convective systems (Markowski and Richardson, 2010; Houze, 2004). Over time, the outflow boundary propagates radially away from the MCS, approaching the AWAKEN region to the northwest.

The cold pool outflow is visible as a fine line in Fig. 2 and as similarly seen for another MCS by Tomaszewski and Lundquist (2021). The fine line in this study represents the front of the atmospheric bore that ultimately reaches the King Plains wind farm. The TTU X-band radars measure

the wind speed over a region encompassing the AWAKEN site, with Fig. 3 showing wind speeds at various heights around 06:30 UTC. Starting at approximately 06:00 UTC on 6 June 2023, oscillations in the wind speed measurement were observed by the X-band radars (see Video 2 in the “Video supplement” section). The oscillations passed through the entirety of the King Plains wind farm at approximately 06:30 UTC. The plan view shown in Fig. 3 has been post-processed to terrain-following heights of 95 (which is close to the 88.5 m turbine hub height), 145, and 270 m a.g.l.

The radar observes bands of faster and slower wind speeds, indicative of wavy turbulence (Fig. 3). In Fig. 3a, at 95 m a.g.l. (near hub height) the wave pattern is not clear, likely because the waves interact with the wind farm and ambient turbulence closer to the surface. However, at 270 m a.g.l. (the highest altitude measured by the radars), the oscillations, seen as alternating color bands stretching left–right across the image, are much more distinct (Fig. 3c). While the gravity waves become weaker closer to the surface, they are faintly visible in Fig. 3b, which represents a height close to the top of the wind turbine rotor layer.

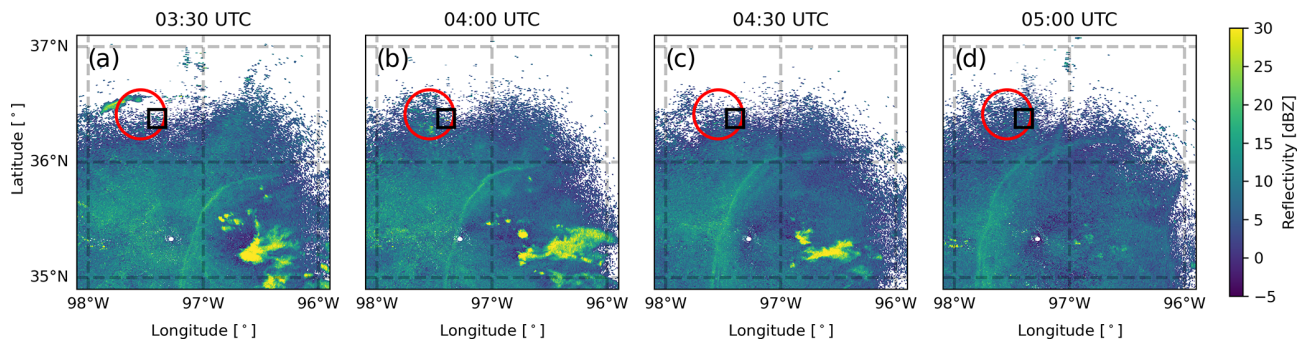


**Figure 2.** NEXRAD WSR-88D radar reflectivity over central Oklahoma at (a) 03:30, (b) 04:00, (c) 04:30, and (d) 05:00 UTC on 6 June 2023. The radar returns are from the Oklahoma City site (KTLX). The area representing WRF domain d02 is outlined in black (see Fig. 4), and the approximate return from the TTU X-band radars is outlined in red. An animation of the NEXRAD data from 03:30–06:00 UTC (22:30–01:00 LT, local time) is included (see Video 1).

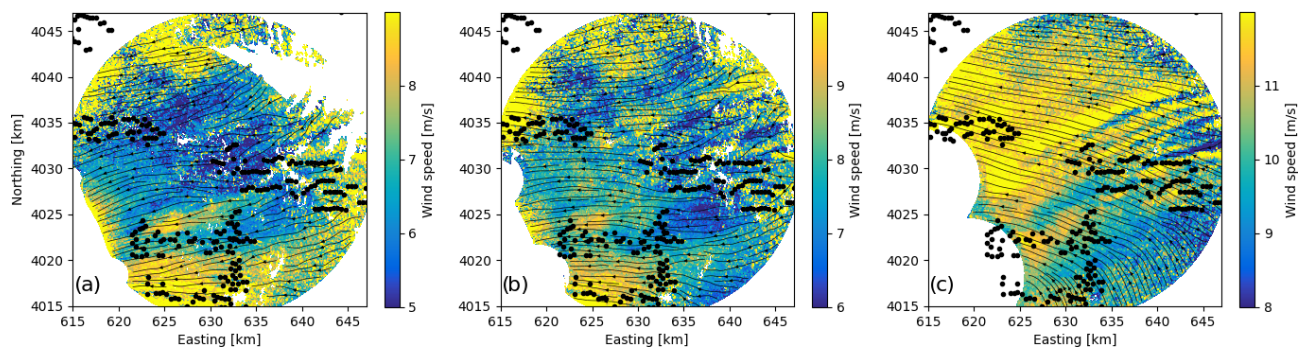


**Figure 3.** Plan view of dual-Doppler wind speed magnitude and streamlines from the TTU X-band radars at 06:27:57 UTC on 6 June 2023 at heights of (a) 95 m, (b) 145 m, and (c) 270 m a.g.l. The timestamp corresponds to the start of the scan routine completed by the radars, which takes approximately 2 min for a full return. An animation of the TTU X-band radar data from 05:30–07:30 UTC is included (see Video 2).

Prior to the bore passage, the ambient atmosphere in the study region can be characterized as stable, as is typical for nighttime conditions in Oklahoma. Time 06:30 UTC corresponds to 01:30 CDT (central daylight time) with sunset occurring nearly 5 h prior at 20:43 CDT. The Obukhov lengths from the surface met station at A1 are 13.8,  $-27.9$ , and  $-23.4$  m at 06:00, 06:30, and 07:00 UTC, respectively, indicating very stable conditions prior to the bore followed by unstable conditions. The passage of the bore perturbs the stable boundary layer, inducing gravity waves that are eventually seen in the measured wind speed measurements in Fig. 3. While the thermodynamic profiling instrumentation from AWAKEN was not online during this specific event, modeling results shown later in this study (see Fig. 6) suggest that the vertical structure of the atmosphere is stably stratified prior to the bore, with an additional discussion on how the bore affects the thermal structure given in Sect. 5.3.

As denoted by the streamlines in Fig. 3, the ambient hub-height wind direction is easterly, a non-ideal wind direction for the King Plains wind farm as the layout was designed for the more dominant southerly wind direction. Interestingly, the gravity waves propagate from the south, which has

a strong influence on the hub-height wind direction as discussed later in this study. Additionally, the hub-height wind speeds are relatively low, on the order of  $4\text{--}6\text{ m s}^{-1}$ , such that the power output of the farm is highly susceptible to wind speed fluctuations in this range (in region 2 of the power curve or in the operational power-maximizing control mode of the wind turbines).

### 3 Methods

#### 3.1 WRF-LES-GAD

The present work uses the large-eddy simulation capability of the WRF model, version 4.4, with modifications including the generalized actuator disk (GAD) (Mirocha et al., 2014), with a turbine yawing capability (Arthur et al., 2020); a stochastic inflow perturbation method (the cell perturbation method, CPM) (Muñoz-Esparza et al., 2014, 2015); and the implementation of a dynamic turbulence closure (Chow et al., 2005; Kirkil et al., 2012). The GAD requires specifications for the turbine's airfoil lift and drag coefficients. However, the required lift and drag parameters for the 2.8 MW General Electric turbines installed at King Plains are not pub-

licly available. We therefore use the open-source 2.8 MW turbine developed by the National Renewable Energy Laboratory (NREL) as a suitable representation in the model, with details available in Quon (2024). The turbine has a hub height of 88.5 m and rotor diameter of 126 m. Minor differences between the NREL turbine and the actual turbines at King Plains are not expected to be critical to the conclusions of this study.

### 3.2 Microphysics parameterizations

In modeling studies involving deep convection, simulation results show sensitivity to the microphysics parameterization (Pandey et al., 2023; Han et al., 2019). Microphysics schemes represent cloud and precipitation processes, describing the formation and growth of water particles (hydrometeors) for clouds, which are especially relevant to the MCS and bore formation in this study. The representation of microphysics in atmospheric models that are cloud-resolving is a major source of uncertainty and an active research area (Morrison et al., 2020; Tatsuya Seiki and Satoh, 2022). The microphysics schemes explored in this study in order of increasing sophistication are the Thompson (Thompson et al., 2008), WRF double-moment 6-class (WDM6) (Lim and Hong, 2010), and Morrison (Morrison et al., 2009) schemes, which are widely used by both operational models and in research. Microphysics schemes largely fall into two categories: single-moment schemes that predict the mixing ratios of hydrometeors and double-moment schemes (WDM6 and Morrison) that predict both the mixing ratio and the number concentration of hydrometeors. The schemes used in this study vary in what prognostic variables or species of particles they predict, which are detailed in Table 1. Note that some double-moment schemes may only be double-moment schemes for a limited number of particle species, as is the case for the Thompson model, which is why the Thompson model is denoted as a 1.5-moment scheme in Table 1. More detail on WRF microphysics schemes can be found in Skamarock et al. (2021).

### 3.3 Turbulence modeling

Extensive literature in LES turbulence closure modeling has shown that dynamic turbulence closures are able to perform better than standard eddy-viscosity approaches in SBL conditions (Zhou and Chow, 2011, 2014; Wise, 2024a). The standard approach to turbulence modeling relies on an implicit filter related to the grid resolution to parameterize the effect of the subgrid-scale (SGS) motions on the resolved flow. In this study, we use an explicit filtering approach to separate large-scale from subfilter-scale motions which provides a framework for using the dynamic procedure of Germano et al. (1991) to solve for coefficients of interest.

When an explicit filter is used, the presence of the numerical grid divides the subfilter-scale (SFS) motions into

resolved and unresolved portions. The unresolved SFS motions are the commonly referred to SGS motions. However, the effect of resolvable subfilter-scale (RSFS) motions can be reconstructed using a scale-similarity approach (see Chow, 2004, for derivations). The RSFS motions are neglected in standard closure schemes (i.e., those that do not use an explicit filter). In this study, we make use of the explicit filtering and reconstruction approach of the dynamic reconstruction model (DRM) turbulence closure (Chow et al., 2005). The performance of the DRM closure with respect to ambient turbulence for this specific case study is compared with other closures in Appendix A.

## 4 Model configuration and description

The two-domain nested setup for WRF-LES-GAD is shown in Fig. 4 with details in Table 2. The setup is unique compared to other multiscale WRF setups in that it uses only two domains, which makes it very computationally efficient. Mesoscale forcing is provided by the High-Resolution Rapid Refresh (HRRR) model v4 (Dowell et al., 2022) as the lateral boundary conditions (updated hourly) for domain d01 following the procedure of Blaylock et al. (2017). The HRRRv4 model was chosen because its horizontal grid spacing is 3 km, which is much finer than the grid resolution used by other regional or global models. In comparison, the Global Forecast System (GFS) (NCEP, 2015) and the European Centre for Medium-Range Weather Forecasts Reanalysis v5 (ERA5) (Hersbach et al., 2020) have grid spacings of 0.25°, which corresponds to roughly 27–28 km. The HRRR 3 km grid spacing is already a very-fine-scale mesoscale simulation, and using a relatively large parent grid ratio of 10 from HRRRv4 to domain d01 is reasonable to intentionally skip across the convective gray zone where turbulence is only partially resolved (Wyngaard, 2004; Chow et al., 2019; Haupt et al., 2019; Muñoz-Esparza et al., 2017).

The HRRRv4 model was also chosen because of its high temporal update frequency and use of data assimilation (DA). The temporal update is hourly, which is important for modeling dynamic events. ERA5 has an hourly temporal update; the GFS has a three hourly temporal update, with forecasts initialized every 6 h. In HRRRv4, Next Generation Weather Radar (NEXRAD) data are assimilated every 15 min during the first hour of simulation, which is referred to as the pre-forecast hour (Dowell et al., 2022). Preliminary simulations were also conducted using GFS and ERA5, which resulted in nocturnal MCSs but in the incorrect location (not shown). In this study, we use the HRRRv4 analysis product which includes assimilated NEXRAD data. Simulations showed that the DA in the HRRRv4 model constrains the initiation of the MCS to the correct location, which is critical to the present study.

Domain d01 is centered over the approximate midpoint between the AWAKEN region and the location where the

**Table 1.** Description of various microphysics schemes used in WRF-LES-GAD.

Parameterization (year published)	Sophistication	mp_physics	Variables
Thompson (2009)	1.5-moment scheme	8	$Q_c, Q_r, Q_i, Q_s, Q_g, N_i, N_r$
WDM6 (2009)	Double-moment scheme	16	$Q_v, Q_c, Q_r, Q_i, Q_s, Q_g, N_n, N_c, N_r$
Morrison (2010)	Double-moment scheme	10	$Q_c, Q_r, Q_i, Q_s, Q_g, N_r, N_i, N_s, N_g$

Mixing ratio of water vapor ( $Q_v$ ); mixing ratios and number concentrations of cloud water ( $Q_c, N_c$ ), rain ( $Q_r, N_r$ ), cloud ice ( $Q_i, N_i$ ), snow ( $Q_s, N_s$ ), and graupel ( $Q_g, N_g$ ); and number concentration of cloud condensation nuclei ( $N_n$ ).

MCS initiates. The 300 m horizontal grid spacing was chosen as a balance between computational cost and model resolution over a large geographic area. Note that preliminary simulations at 1 km grid spacing did not provide a realistic bore structure (not shown). Additional preliminary simulations at 200 m grid spacing provided similar results as those with the 300 m grid spacing (not shown), which is consistent with the findings of Johnson and Wang (2019), who found little benefit to increasing the grid resolution beyond 250 m for their bore simulations. As previously mentioned, modeling studies that resolve deep convection show large sensitivities to cloud and precipitation processes. Therefore, three separate simulations for domain d01 are run with the microphysics schemes specified in Table 1 with results compared in Sect. 5.1.

Domain d02 has 20 m horizontal grid spacing, which is necessary to resolve the effects of individual wind turbines using the generalized actuator disk parameterization. The 20 m horizontal grid spacing is fine enough to include six grid points across each generalized actuator disk in the horizontal (and 16 in the vertical with the grid spacing described in Table 2). The GAD parameterization is typically used at 10 m spacing (Mirocha et al., 2014; Arthur et al., 2020; Wise et al., 2022), but given the large domain size required here, preliminary simulations showed that 20 m horizontal grid spacing provides reasonable results. When using 20 m grid spacing, and prior to the turbulent mixing in the far-wake region, the near-wake structure importantly still retains the characteristic bimodal distribution of the velocity deficit (also described as a double-Gaussian velocity deficit in Keane et al., 2016, and Schreiber et al., 2020). The bimodal distribution is due to blade geometry and aerodynamics, as well as nacelle effects as seen in experiments, observations, and modeling (Wang et al., 2017; Vermeer et al., 2003; Carbajo Fuertes et al., 2018).

A parent grid ratio of 15 from d01 to d02 bridges the MCS-resolving domain (domain d01) to the turbine-wake-resolving domain (domain d02). Intermediate nests with grid spacings between 300 and 20 m were explored but found to lessen the agreement with observations (not shown) as in Mazzaro et al. (2017). Because of the large parent grid ratio between domains d01 and d02, the development of small-scale turbulent structures on d02 is accelerated using the cell perturbation method (CPM), a stochastic inflow perturbation

method (Muñoz-Esparza et al., 2014, 2015). The CPM works by applying small temperature perturbations at the domain boundaries, fostering the development of a wider range of turbulent scales with negligible computational cost. CPM has been used successfully in a large number of WRF-LES studies (Arthur et al., 2020; Connolly et al., 2021; Wise et al., 2022; Sanchez Gomez et al., 2022, 2023).

At 20 m grid spacing, much of the ambient turbulence is resolved on d02; however, SBL conditions tend to reduce the turbulent length scale. Previous work has shown that dynamic turbulence closures can resolve more ambient turbulence compared to standard closures at coarser grid resolutions, especially in strongly stable conditions (Zhou and Chow, 2011, 2014; Wise, 2024a). Therefore, the DRM closure is especially well suited for this case study and simulation setup. The sensitivity of resolved turbulence characteristics to the turbulence closure is explored in Appendix A.

Because of the computational expense of these simulations, the start time of domains d01 and d02 is staggered. Domain d01 begins on 6 June 2023 at 03:00 UTC, which is just over 3 h prior to the gravity wave reaching the measurements at the AWAKEN site. A 3 h lead time is chosen following the favorable results from the forecast start-time sensitivity conducted by Johnson and Wang (2017). Domain d02 begins at 05:00 UTC and is run until 07:30 UTC with the first hour (05:00–06:00 UTC) considered to be spin-up time and therefore not used in the analysis. With both domains running concurrently, 30 min of simulation time takes approximately 24 h of wall-clock time on 800 cores.

WRF-LES-GAD is run using a third-order Runge–Kutta time advancement scheme, with fifth-order horizontal and third-order vertical advection schemes. The physical parameterizations are as follows: the Noah land surface model (Chen and Dudhia, 2001), the Rapid Radiative Transfer Model for longwave radiation (Mlawer et al., 1997), and the Dudhia shortwave radiation model (Dudhia, 1989). No cumulus parameterization option is used as convection is explicitly resolved using LES.

For the turbulence closure, on domain d01, we use the standard turbulent kinetic energy 1.5-order (TKE-1.5) LES closure (Deardorff, 1980). On domain d02, where ambient turbulence is resolved and the wind turbines are parameterized, we use the DRM LES closure (with comparisons using other closures shown in Appendix A). All domains use the

**Table 2.** Parameters used for the nested multiscale WRF-LES-GAD setup. For the vertical resolution,  $\Delta z_{\min}$  is for the first grid point above the surface and is approximate due to the nature of the terrain-following coordinate system in WRF. MYNN-EDMF is the Mellor–Yamada–Nakanishi–Niino eddy-diffusivity mass-flux scheme (Olson et al., 2019).

Domain	$\Delta x$ [m]	Grid ratio	$\sim \Delta z_{\min}$ [m]	$N_x \times N_y$	$\Delta t$ [s]	Turbulence closure
Forcing	3000	–	15	$1800 \times 1060$	20	MYNN-EDMF
d01	300	10	8	$1200 \times 1200$	1.5	TKE-1.5
d02	20	15	8	$661 \times 871$	0.1	DRM

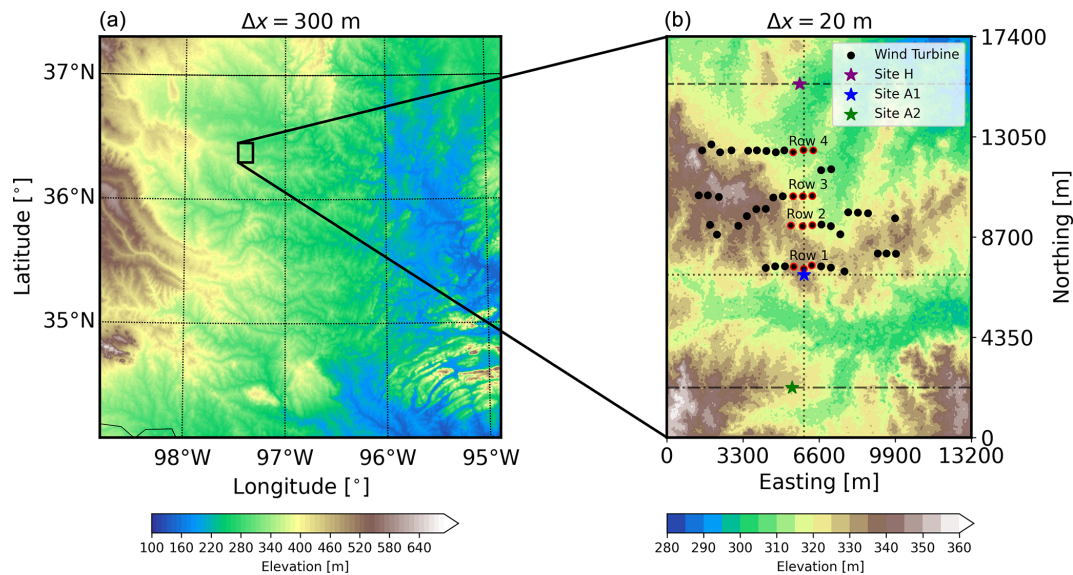


**Figure 4.** Topography of domains (a) d01 and (b) d02 used in the multiscale simulation. Dimensions of each domain and other configuration information are included in Table 2. Note that the two plots have different ranges for their color bars due to the maximum and minimum elevations within each domain.

eta similarity surface layer scheme (Janjić, 1994), which uses similarity theory (Monin and Obukhov, 1954) to determine the relevant surface fluxes. For topography, high-resolution terrain data (1 arcsec, approximately 30 m) are used from the Shuttle Radar Topography Mission (Farr et al., 2007). The land-use data similarly use 30 m spacing; they are from a National Land Cover Database product converted into USGS categories (as in Chen et al., 2024). The domain extends 20 km above the ground; at the upper-boundary condition, diffusive damping is applied with a coefficient of 0.01 following Johnson et al. (2018).

## 5 Results and discussion

### 5.1 Bore structure sensitivity to microphysics parameterizations

The case study examined in the present work is an atmospheric bore event with associated gravity waves that were observed to interact with the King Plains wind farm on 6 June 2023. The development of the bore is highly sensitive to the selected microphysics parameterization. Figure 5

shows the vertical velocity at 1 km a.g.l. and the potential temperature at 200 m a.g.l. for 04:00 UTC, which is 1 h after the simulation/forecast start time. All three microphysics parameterizations resolve the deep convection and look qualitatively similar. Subtle differences in the strength of the cold pool, however, ultimately affect the development of the bore as it propagates roughly 100 km to the AWAKEN region.

The cold pool generated by the MCS is governed by latent cooling from the downdraft generated due to precipitation. The precipitation partially evaporates which produces the colder air downdraft, which forms the cold pool (Markowski and Richardson, 2010; Muller and Abramian, 2023). The cold pool then spreads horizontally as a density current when it reaches the surface. Planar-averaged vertical profiles of potential temperature and various hydrometeor species within the MCS are shown in Fig. 6. The subdomain that encompasses the MCS is shown in Fig. 5. The thermal structure of the MCS is similar for the three different microphysics parameterizations; however, results with the WDM6 microphysics are colder from the surface up to 3 km a.g.l. The stronger cold pool for the WDM6 microphysics scheme compared to the other schemes is because below the cloud base

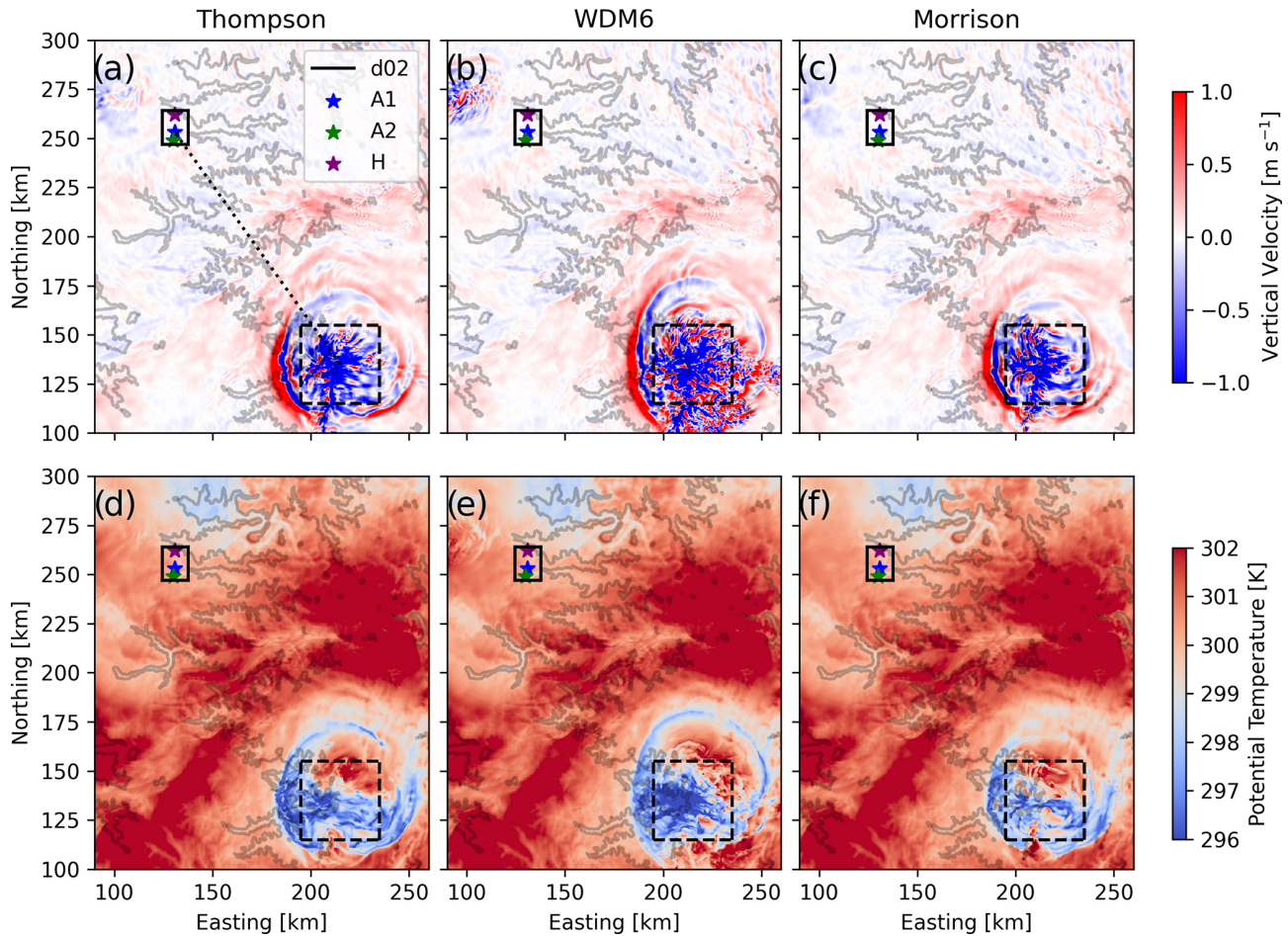


**Figure 5.** Instantaneous plan slice of (a–c) vertical velocity at 1 km a.g.l. and (d–f) potential temperature at 200 m a.g.l. on domain d01 for various microphysics schemes. Line contours represent 100 m changes in elevation. Note that the domain has been cropped for visualization purposes. A subdomain is denoted as the dashed box, which is used for analysis in Fig. 6. The dotted line in (a) is a transect used for the visualization in Fig. 9.

(approximately 2 km a.g.l.; see Fig. 6b), the rain water mixing ratio decreases with decreasing altitude. The decrease in rain water mixing ratio indicates low-level rain evaporation as discussed by Johnson et al. (2018), which provides latent cooling. Both the Thompson and Morrison microphysics schemes have relatively constant rain water mixing ratios below the cloud base. Another contributing factor to the differences in the thermal structure of the MCS is the larger snow water mixing ratios in the upper atmosphere above the cloud base, which, in-turn, reduce the graupel and rain water mixing ratios. These trends are similar to those found by Johnson et al. (2018) in their microphysics sensitivity study.

In contrast with Johnson et al. (2018), only the WDM6 microphysics scheme provides realistic bore structure by the time it reaches the AWAKEN region. Time–height contours in Fig. 7 show vertical profiles of wind speed and vertical velocity for the three different microphysics parameterizations compared with the lidars at A1. Note that the observations in Fig. 7a and b include both the Halo XR+ lidar,

which measures from 100 m a.g.l. to the top of the boundary layer but with an alternate scan schedule every 20 min, and the WindCube v2, which focuses on lower altitudes measuring from 40 to 240 m a.g.l. While there are faint wavy structures in the simulation results using Thompson or Morrison, only WDM6 provides gravity waves that resemble observations and is therefore selected for further analysis. With WDM6, the period of the initial wave is  $\sim 5$  min in the model compared to  $\sim 4.5$  min for the observations as defined by the time between the first two wind speed peaks. There is a 16 min delay in the timing of the bore for the results with WDM6 compared to observations, likely due to small differences in the bore speed with the gravity waves first appearing at 06:09 UTC in observations compared to 06:25 UTC in the model. Considering that the bore propagates over 100 km from the MCS to the AWAKEN region, for example, a difference in the bore speed of  $1 \text{ m s}^{-1}$  can result in a timing difference of nearly 20 min. Additionally, the bore propagation speed is not necessarily constant with time as it can

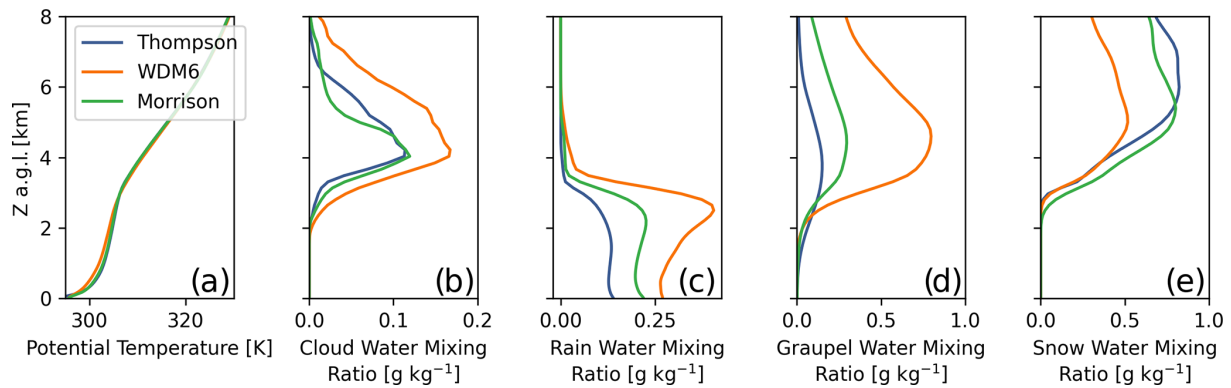


**Figure 6.** Vertical profiles averaged in the subdomain from Fig. 5 for (a) potential temperature, (b) cloud water mixing ratio, (c) rain water mixing ratio, (d) graupel water mixing ratio, and (e) snow water mixing ratio for the various microphysics schemes.

be affected by the ambient environment (Johnson and Wang, 2017; Haghi et al., 2019).

The mesoscale environment is very similar regardless of microphysics scheme. Figure 7 shows that a low-level jet (LLJ) exists prior to the bore passage. The maximum wind speed in the LLJ is predicted accurately by the model at 270 m a.g.l. as was observed; however, there is a positive bias in the wind speeds predicted by the model. These differences can be quantified by time averaging the flow prior to the gravity waves (05:30–05:50 UTC for the observations and 05:46–06:06 UTC for the model accounting for the time delay). Specifically, for results using WDM6, the model predicts a LLJ maximum wind speed of  $10.2 \text{ m s}^{-1}$ , whereas the observed maximum wind speed by the Halo XR+ lidar is  $9.3 \text{ m s}^{-1}$ . During the same time period, the model-predicted hub-height wind speed is  $5.5 \text{ m s}^{-1}$ , whereas the observed hub-height wind speed by the WindCube v2 lidar is  $4.7 \text{ m s}^{-1}$ . These errors in the wind speed are likely because of differences in the HRRRv4 forcing used as the lateral boundary conditions. Importantly, the wind direction at hub height is well predicted by the model at  $54.5^\circ$ , whereas the observed wind direction is  $51.4^\circ$ . Notably, the LLJ is weakened after the bore passage, which is discussed in more detail later.

The vertical velocity and wind speed signals in Fig. 7 are highly correlated during the gravity wave passage. During an updraft or downdraft of the wave, there is a corresponding convergence or divergence in the horizontal velocity. In Fig. 7e and f, there are two strong peaks followed by residual wavy structures with less intensity. In the observations, there are three strong peaks which are followed by a 10 min period of missing observations due to an alternate scan schedule for the Halo XR+ lidar. The observations are typical for bores where there are strong initial waves followed by elevated turbulence along with a lifting of the boundary layer (Haghi et al., 2019; Haghi and Durran, 2021), which is discussed in more detail in the following sections. It is also important to note that the gravity waves manifest most strongly in the

wind speed signal at heights from 200–800 m a.g.l. The intensity of the gravity waves in the wind speed signal diminishes closer to the surface and toward the top of the rotor layer, which was also found to be true in the radar measurements (Fig. 3).

## 5.2 Gravity wave characteristics and evolution

The MCS-induced cold pool propagates outward, which perturbs the stably stratified atmosphere as a bore. The progression of a bore is well described in Haghi et al. (2017) with the bore in the present study falling between a bore with undulations and one with solitary-like waves by the time the bore reaches the AWAKEN site. Note that all results presented in this paper hereinafter use the WDM6 microphysics scheme. Figure 8 shows instantaneous plan slices at 30 min increments for the vertical velocity at 1 km a.g.l. and the potential temperature at 200 m a.g.l. on domain d01. The height of 1 km a.g.l. is standard for studies involving bores, while 200 m a.g.l. represents a height closer to the surface and also where the cold pool is very strong. At 05:00 UTC, the bore forms a ring as it propagates outward and spreads radially from the parent MCS. As the bore moves closer to the AWAKEN region, it gradually mixes into the ambient environment. While the strength of the cold pool weakens the further it travels from its parent MCS, gravity waves continue to propagate in the thermally stratified atmosphere as evident in Fig. 8. At 05:00 UTC, there is a clear leading wave, and by 05:30 UTC, trailing waves are seen forming a wave train. The wave train reaches the AWAKEN region at 06:30 UTC with two large waves followed by a number of additional waves in the train. The waves then weaken in intensity at 07:00 UTC.

The vertical structure of the atmosphere is substantially impacted by the propagating bore and associated wave train. Figure 9 shows a vertical cross-section, along the transect illustrated in Fig. 5a, of the wind speed and potential temperature at the same time increments as in Fig. 8. Note that the color bar in Fig. 9 is specifically chosen to highlight the

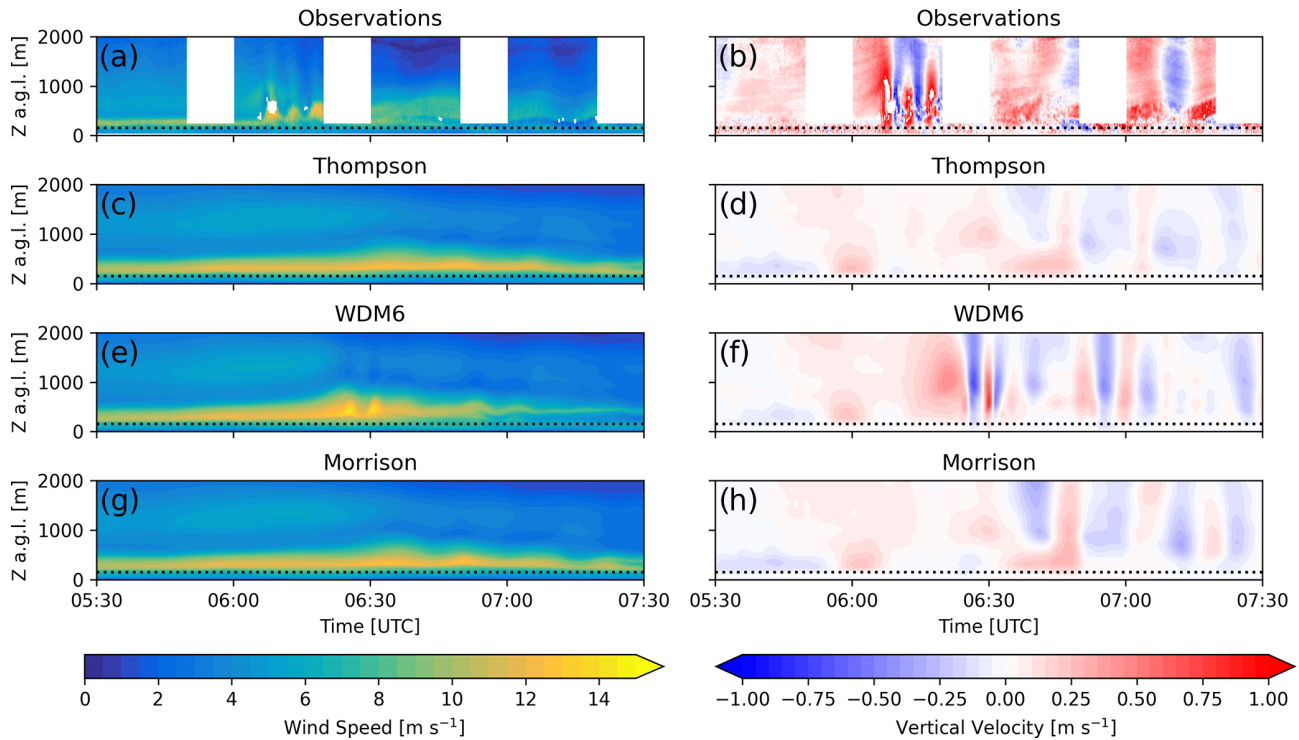


**Figure 7.** Time–height contours of wind speed and vertical velocity in (a, b) observations from the lidars and (c–h) the model for various microphysics schemes all at Site A1. The dotted line corresponds to the top of the wind turbine rotor layer.

colder temperatures which form the SBL (but note that the entirety of the atmosphere in Fig. 9 is stably stratified). At 05:00 UTC (Fig. 9a and b), the bore is evident as an injection of faster wind speeds and colder temperatures into the transect with the density current traveling in the positive direction. Initially, the colder temperatures in the bore appear most clearly as a singular front that perturbs the SBL. Over time, the front evolves into a number of wavy structures at the interface of the SBL and free atmosphere that form the wave train. Additionally, the bore itself increases the height of the SBL, which is discussed in more detail in Sect. 5.4.

In the wind speed signal, the interaction between the bore and ambient environment is more complex. At 05:00 UTC (Fig. 9a) and upwind of the density current (distances  $> 100$  km), there is a preexisting east-northeasterly LLJ with a height of 600 m a.s.l. and a maximum wind speed of  $10 \text{ m s}^{-1}$ . Also evident in Fig. 9a is the wind speed behind the bore front, which is greater than  $14 \text{ m s}^{-1}$ . Over time, the wind speeds within the bore weaken substantially from as high as 14 to  $6\text{--}8 \text{ m s}^{-1}$ . However, the bore continues to propagate in the positive direction, which results in the advection of the preexisting LLJ in the positive direction. By 06:30 UTC (Fig. 9g), the effect of the bore on the preexisting LLJ manifests itself as two well-defined waves in the wind speed signal (with a number of additional wavy structures behind the front). These two maxima result in the clear, distinct waves in the time–height contours at A1 (Fig. 7e) that

occurred 5 min after each other. The distance between the well-defined maxima is 4.5 km. Trailing waves are also evident in Fig. 9g and h but are much slower in wind speed and also have larger distances between the waves. By 07:00 UTC (Fig. 9i), the effect of the bore is that the LLJ no longer extends into the AWAKEN region, and, as a result, the wind turbines at King Plains experience much slower wind speeds. The effect of this modulation of the mesoscale environment by the bore is further quantified in Sect. 5.4.

### 5.3 Bore and gravity wave effects on the boundary layer

The gravity waves associated with the bore are strongest higher in the atmosphere. Vertical slices of wind speed and vertical velocity for domain d02 are shown at various times during the gravity wave passage in Fig. 10. The vertical slices are taken along a north–south transect that intersects point A1 shown in Fig. 4. This transect intersects four rows of the King Plains wind farm, but since the hub-height winds are more northeasterly, wakes are largely out of plane in Fig. 10. At 06:25 UTC, the first wave of the solitary-like wave train, which has a wave-to-wave time interval of 5 min and physical distance of 4.5 km, is seen approaching the wind farm in Fig. 10a and d. As time progresses, there are a number of additional waves that pass over the wind farm. While the gravity waves are the dominant feature above the wind turbines, there are other turbulent features related to wakes and

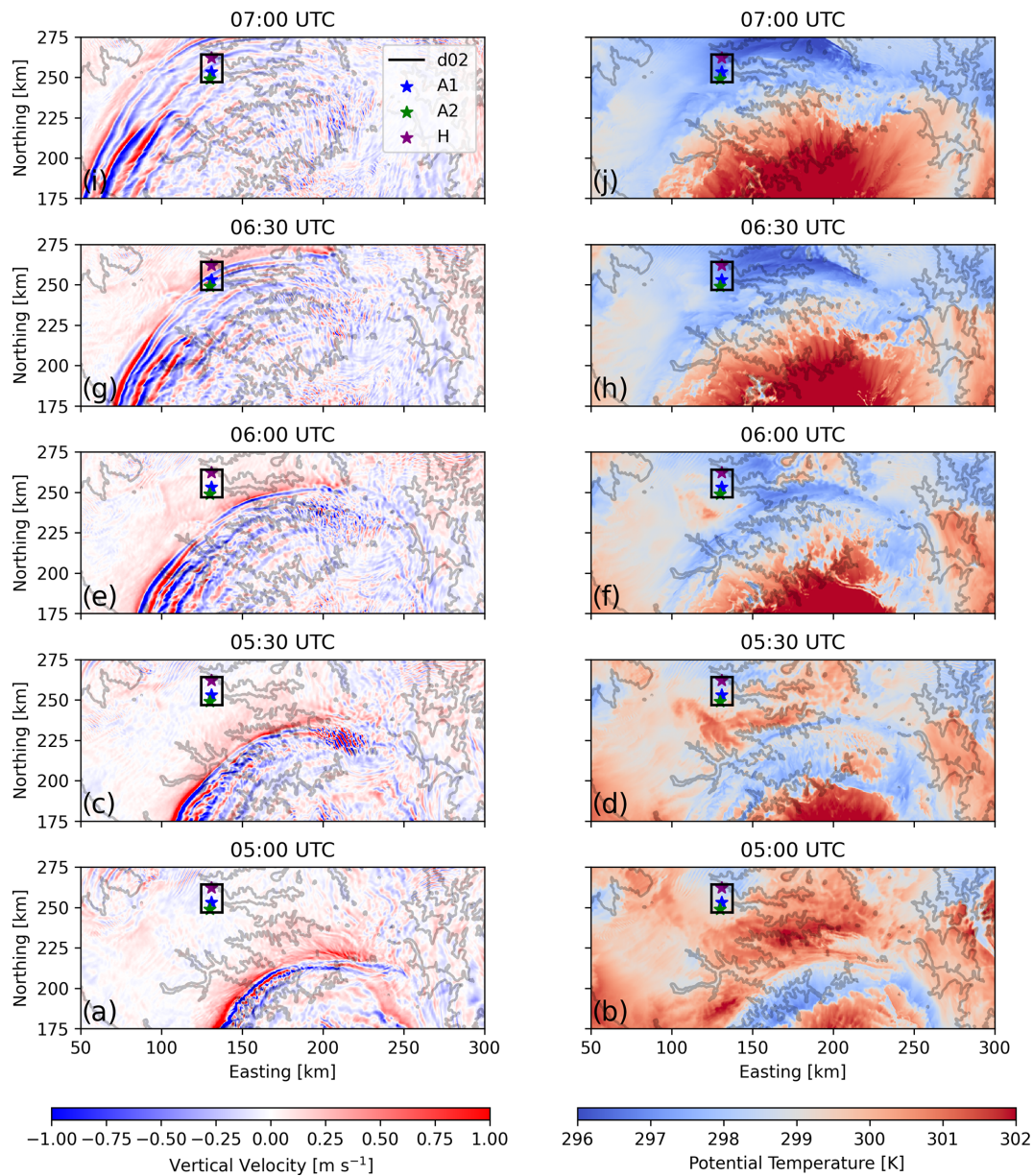


**Figure 8.** Plan slice of (a–e) vertical velocity at 1 km a.g.l. and (f–j) potential temperature at 200 m a.g.l. from 05:00 to 07:00 UTC in 30 min increments on domain d01. Line contours represent 100 m changes in elevation. Note that the domain has been cropped for visualization purposes and that the panels progress in time from bottom to top to highlight the northward movement of the bore. An animation of modeling results is included (see Video 3).

ambient turbulence in the rotor layer and closer to the surface.

Vertical profiles provide a more quantitative understanding of how the structure of the atmosphere is modulated by gravity wave–wind farm interactions. Figure 11 shows vertical profiles of time-averaged wind speed, wind direction, potential temperature, and resolved heat flux at Site A1. At Site A1, model results are compared against both profiling (closer to the surface) and scanning (higher up in the atmosphere) Doppler lidar measurements of the wind speed. The

vertical profiles are time-averaged for periods before, during, and after the gravity wave passage. The averaging windows used depend on the specific site due to the time it takes for the gravity waves to propagate northward. We assume that the gravity waves propagate at a speed equal to the wave-to-wave physical distance (4.5 km) divided by the time interval (5 min), which is 15 m s<sup>-1</sup>. Additionally, because there is some difference in when the wave arrives in the model compared to the measurements, there is a 16 min shift used when defining these periods for the measurements compared

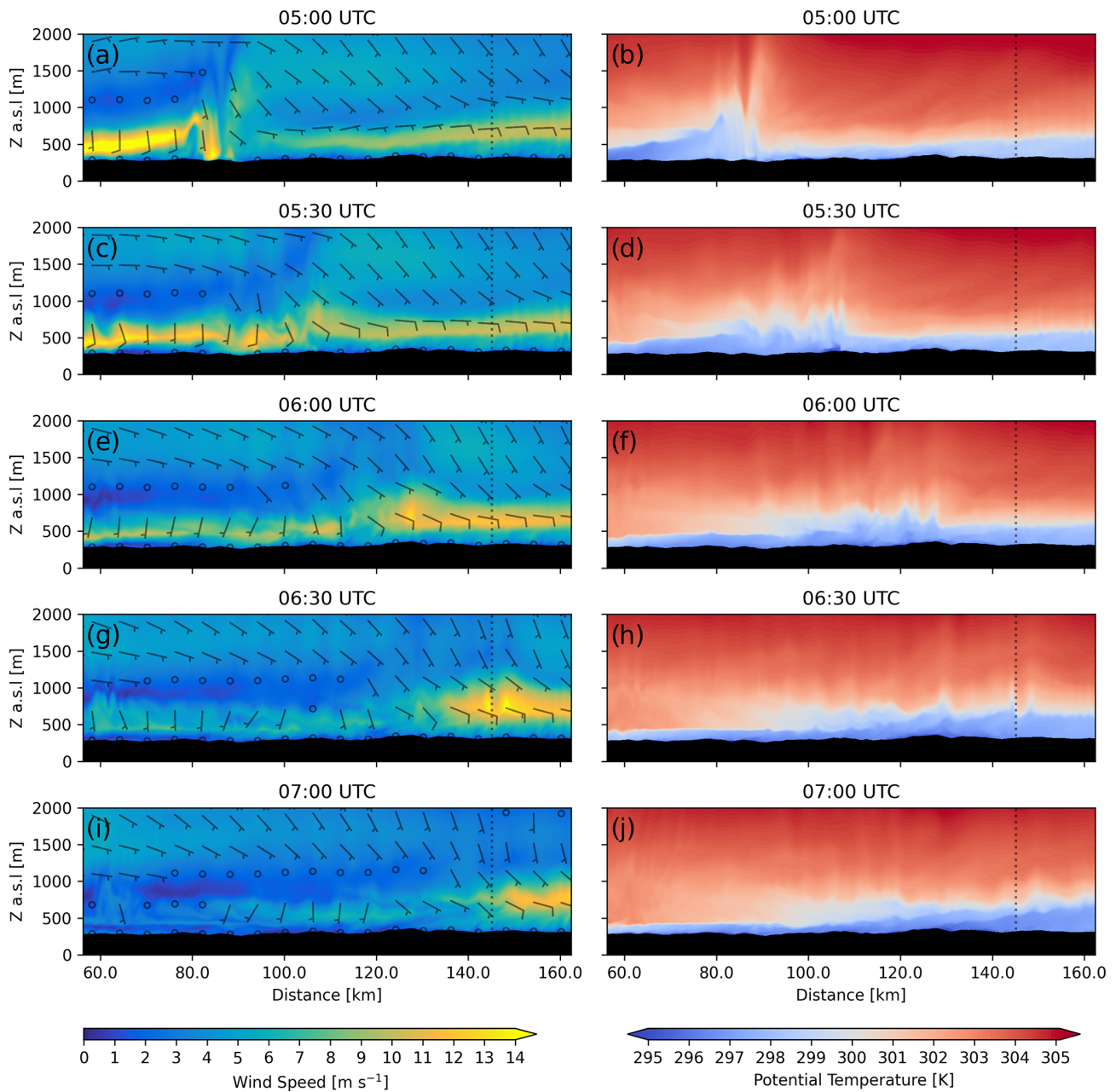


**Figure 9.** Vertical cross-section of wind speed (with wind barbs) and potential temperature from 05:00 to 07:00 UTC in 30 min increments. The transects are along the dashed line shown in Fig. 5. The dotted line corresponds to the location for Site A1.

to the model (as was done when similarly analyzing a MCS by Tomaszewski and Lundquist, 2021). For example, the averaging window used for “during” is 06:04–06:34 UTC at Site A1 for the measurements, while it is 06:20–06:50 UTC for the model. The averaging periods used to generate the vertical profiles are summarized in Table 3.

The measurements and modeling results demonstrate the weakening and eventual destruction of the LLJ due to the propagating gravity waves generated by the MCS. In the vertical profiles of wind speed (Fig. 11a), there is a well-defined

maximum above the rotor layer (representing the LLJ nose) prior to the gravity waves. During the gravity wave passage, the vertical location of the LLJ nose increases in height, and after the gravity waves, the LLJ maximum is significantly diminished. But the wind speed maximum of the LLJ and the negative shear region above are both overestimated in the model. However, in both observations and the model, the LLJ itself does not recover beyond the “after” analysis period prior to sunrise (not shown). In addition to the decrease in wind speed due to the gravity waves, the wind direction also

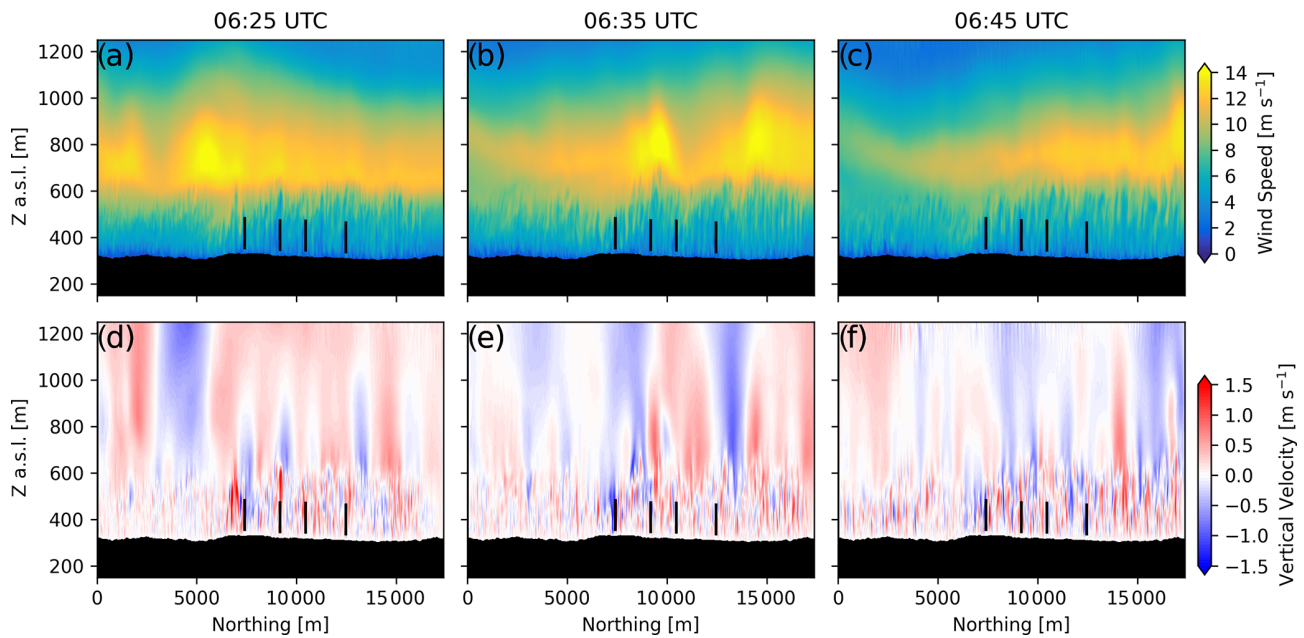


**Figure 10.** Instantaneous vertical cross-sections of (a–c) wind speed and (d–f) vertical velocity along the A1 north–south transect at various times during the gravity wave event.

**Table 3.** Time windows used for averaging vertical profiling results when comparing WRF-LES-GAD with observations at Site A1.

	Before	During	After
Measurement averaging window (UTC)	05:34–06:04	06:04–06:34	06:34–07:04
Model averaging window (UTC)	06:00–06:20	06:20–06:50	06:50–07:20

becomes more easterly as shown in Fig. 11b. Before the gravity waves arrive, the wind direction is east-northeasterly (approximately  $60^\circ$ ) at hub-height, with substantial wind veer across the rotor layer. During and after the gravity wave passage, the wind direction is more easterly, which is suboptimal for the east–west rows of the King Plains wind farm, due to waking within the row. The bore and the associated gravity waves advect from the south-southeast, which forces the ambient northeasterly winds to become more easterly. The effect of the gravity waves on the wind direction is discussed further below.

The thermal structure of the atmosphere is also strongly impacted by the gravity wave passage. Prior to the gravity wave arrival, the boundary layer is stably stratified up to approximately 200 m, above which the atmosphere is more stable. In Fig. 11c, the boundary layer height is increased during the gravity wave passage. The increased boundary layer height persists even after the gravity wave passage, which is a common characteristic of bore events (Haghi et al., 2019; Haghi and Durran, 2021). In addition to the boundary layer height increasing, the boundary layer cools and the thermal stratification weakens during the gravity wave passage, and these changes also persist after the wave passage. The sta-

bility weakening was also observed by the sonic anemometers at the A1 surface met station as previously discussed in Sect. 2.1. The cooling and deepening of the boundary layer are driven in part by the advection of colder temperatures into the region by the bore itself. Additionally, as the gravity waves pass, there is a positive heat flux in the upper atmosphere (Fig. 11d), indicating that heat is transferred from lower altitudes to higher altitudes, thus weakening the thermal stratification.

#### 5.4 Gravity wave–wind farm interaction

The effect of the gravity waves on the power production of the King Plains wind farm is twofold. First, the destruction of the LLJ by the gravity waves results in a decrease in the average power production. Second, there is increased power variability during the gravity wave passage. Figure 12a shows a time series of the simulated power production of the wind farm by row, with the power signal smoothed to reduce noise by applying a 1 min running average. Figure 12b shows a time series of the observed power production for row 1 from the SCADA data, with the power data normalized at the request of the wind farm operator. The King Plains wind farm layout is nonuniform and as a result, there are certain rows

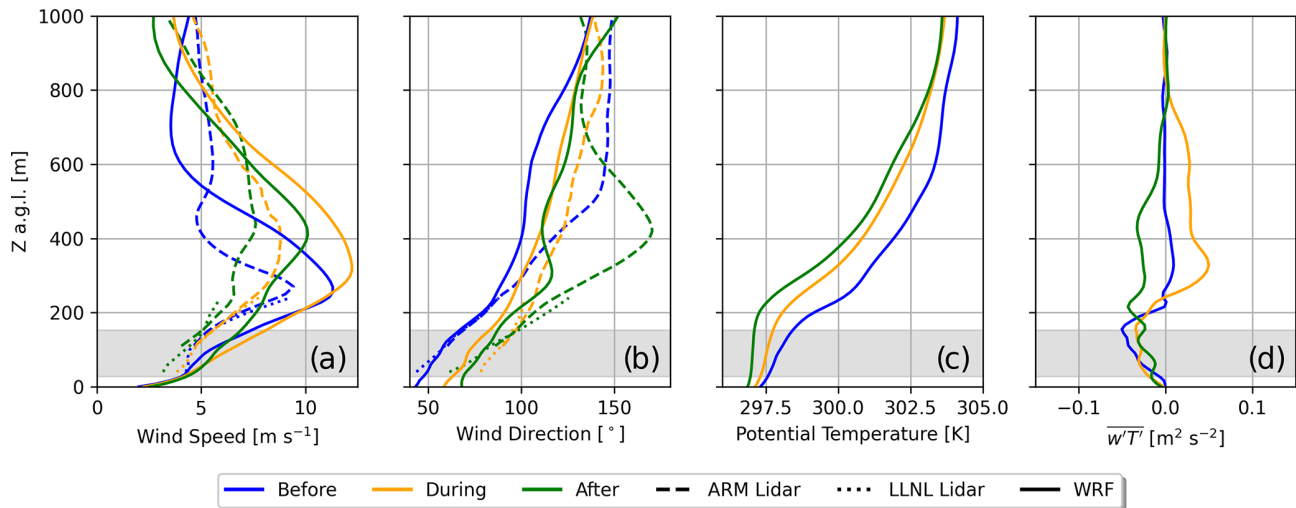


**Figure 11.** Time-averaged vertical profiles of (a) wind speed, (b) wind direction, (c) potential temperature, and (d) resolved heat flux for observations and simulation results at Site A1. See Table 3 for the averaging windows. The wind turbine rotor layer is highlighted in gray.

with more wind turbines than others. In an attempt to equalize this factor, three turbines in each row are selected as shown in Fig. 4. Additionally, because the gravity wave propagation direction and turbine rows are slightly misaligned, only the three middle turbines from each row are considered to quantify the coherent effect of the gravity waves on individual turbines. In Fig. 12, the period during which the turbines are most significantly impacted by the gravity waves is highlighted in gray (06:25–06:55 UTC). For the simulated power, prior to the gravity waves, the first row of turbines averages 1.54 MW of power, whereas after the gravity waves have modulated the mesoscale environment, the first row of turbines averages 44 % less power at 0.86 MW. All rows of turbines produce less power after the gravity waves pass, with row 2 producing 56 % less power, row 3 producing 34 % less power, and row 4 producing 15 % less power on average. Row 1 has the largest increase in power variability during the gravity wave passage. The standard deviation increases by over 100 % for row 1 from 0.18 MW prior and 0.16 MW after the gravity waves to 0.42 MW during the gravity wave passage. The power variability in the other rows is not as notable.

The SCADA data qualitatively confirm many of the trends in the simulated power production in Fig. 12. The power output of all rows decreases after the gravity wave passage. The SCADA data similarly show power variability due to the gravity waves (in the gray region). However, there are differences in the variability on timescales shorter than that of the gravity waves, due to differences between the actual and simulated turbine controller. The simulations and SCADA data both show clear effects of the gravity waves in the power signal for row 1, but for rows 2–4 (especially rows 3 and 4), the gravity wave effects are more extreme in the SCADA compared to the simulation results. A potential reason for this dif-

ference is that the observed gravity waves could contain more energy than those predicted by the model. In the model, the gravity waves near the surface are dissipated as soon as they encounter the first row of the wind farm. In reality, the more energetic gravity waves are likely able to entrain momentum from above such that their effect is felt more strongly throughout all four rows. Considering the good agreement between the simulated and observed power signals for row 1, the model is able to capture the leading edge of the gravity wave passage but likely overestimates the dissipative effect of the wind farm on the gravity waves. Lastly, it is important to note that subtle differences in the wind direction can cause large power fluctuations due to waking because of the configuration of the farm (as discussed in the following paragraphs).

The increased power variability during the gravity wave passage is due to oscillations in the wind speed magnitude (mainly for row 1) as well as due to an indirect effect, related to subtle shifts in the wind direction caused by the wave motion. Figure 13 shows the simulated power signal in rows 1 and 2 along with the local perturbation pressure and wind direction signals. The perturbation pressure represents the total atmospheric pressure with the base pressure removed (Skamarock et al., 2021). The local hub-height perturbation pressure and wind direction signals are obtained by spatially averaging a 600 m × 600 m area centered over the middle turbine within each row. At the beginning of the period affected by the gravity waves, there are two peaks in the pressure signal which correlate to the waves in Fig. 7. The wind direction also correlates with the perturbation pressure signal, with higher perturbation pressure corresponding to more easterly wind and lower perturbation pressure corresponding to more east-northeasterly winds.

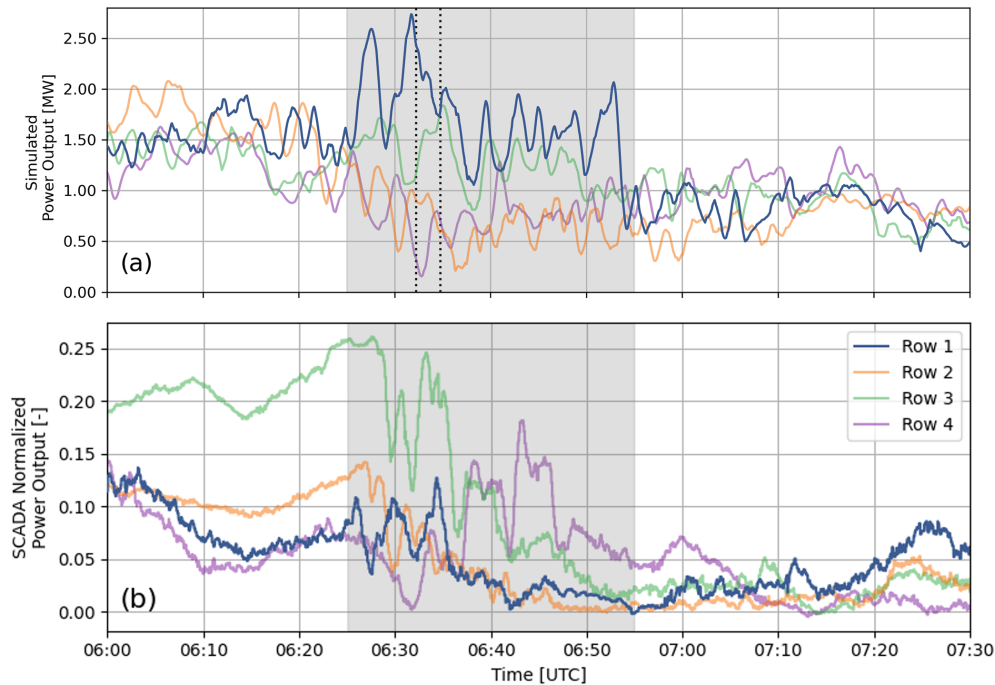


**Figure 12.** (a) Time series of simulated row power outputs for the eastern King Plains wind farm from 06:00 to 07:30 UTC. The dotted lines in (a) highlight the time instants shown in Fig. 14. (b) Time series of SCADA normalized row power outputs. Because of the delay in when the gravity waves arrive in the model compared to observations, the SCADA data were shifted by 16 min. Figure 4 shows the turbines that represent each row.

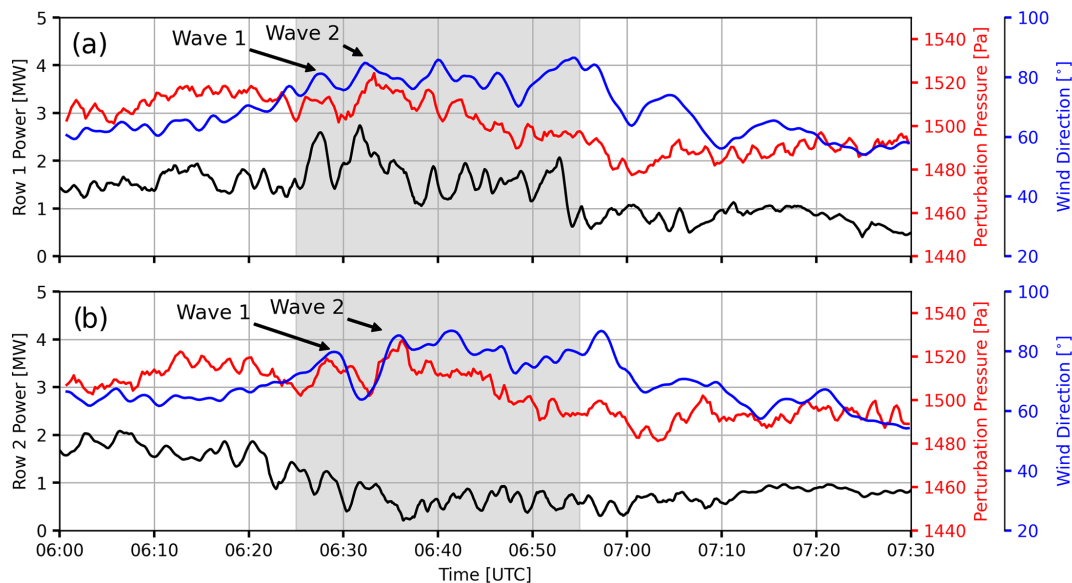


**Figure 13.** Time series of the simulated (a) row 1 and (b) row 2 local wind direction, perturbation pressure, and power for the eastern King Plains wind farm from 06:00 to 07:30 UTC.

The correlation of the hub-height wind direction and perturbation pressure is qualitatively more clear in a plan view. Figure 14 shows the wind speed and perturbation pressure at hub height along with streamlines at two different time instances. Closer to the surface, the gravity waves manifest

most clearly in the perturbation pressure signal. The two time instances were chosen to display the effect of high- and low-pressure regions beneath the gravity waves. During the first time instance (06:32:15 UTC), the second row of turbines is in a low-pressure region and is experiencing wind directions

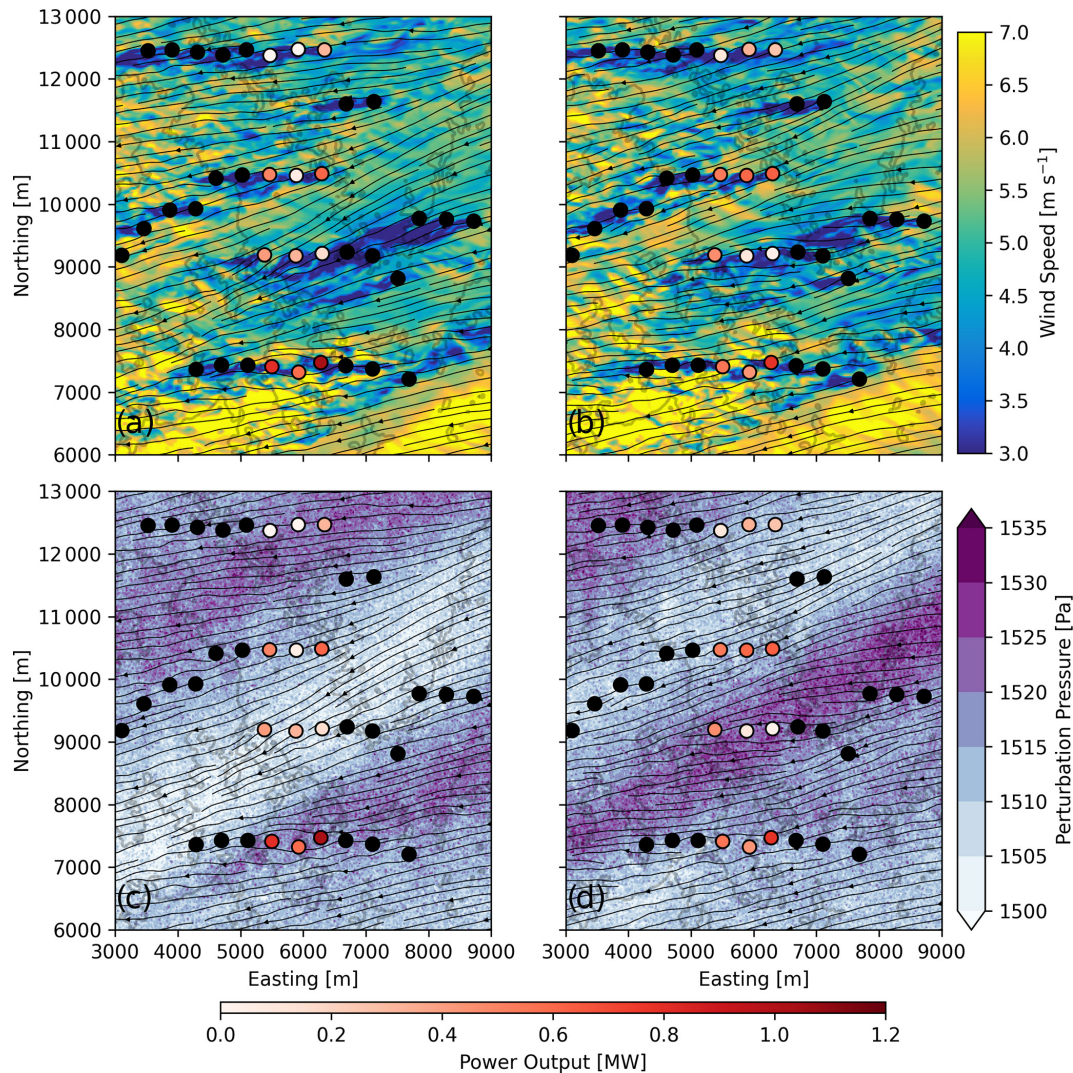


**Figure 14.** Instantaneous plan view of hub-height wind speed and perturbation pressure at (a, c) 06:32:15 UTC and (b, d) 06:34:45 UTC. The streamlines correspond to the hub-height wind speed; however, note that the gravity waves are advecting northward. An animation of modeling results is included (see Video 4).

that are more east-northeasterly. During the second time instance (06:34:45 UTC), the second row of turbines is in a high-pressure region and the wind direction is easterly. The same relationship between pressure and wind direction is observed beneath the gravity waves. More easterly winds are less favorable for the King Plains layout and result in significant power losses due to wakes.

The second row of turbines produces more power during the first time instance with the east-northeasterly winds at 0.90 MW, while the same row produces 34 % less power during the second time instance with easterly winds. A similar, but opposite, trend happens for row 4 related to the wave-to-wave distance of the waves. During the first time instance, the majority of the turbines in row 4 experience wakes during the easterly wind directions, and the row is producing just 0.32 MW of power. The turbines in row 4 experience more

east-northeasterly wind directions during the second time instance and are thus producing more power at 0.71 MW.

While the gravity waves induce wind direction shifts which modulate the produced power, it is important to remark that the power production in the farm is variable due to additional factors. Importantly, local turbulent structures have a strong impact on the wind speed experienced by turbines that increase or decrease power. Additionally, these local turbulent structures induce wake meandering and, given the non-optimal wind directions for the layout, can increase or decrease turbine power production depending on whether they are being waked or not.

## 6 Conclusions

In this study, WRF-LES-GAD is used to understand wind farm impacts from gravity waves observed on 6 June 2023 during the American Wake Experiment (AWAKEN) field campaign. The case study was initially characterized using X-band and NEXRAD weather radars as these devices measure very large geographical extents. The gravity waves were determined to be associated with an atmospheric bore event, which was generated by nocturnal mesoscale convection near the AWAKEN site. A cold pool, which formed as a result of precipitation-induced latent cooling within the mesoscale convective system (MCS), began to spread radially as a density current or bore. A train of solitary-like waves formed at the front of the bore, interacting with the preexisting stable boundary layer in the study region and ultimately passing through the King Plains wind farm.

To model the bore and its associated gravity waves, we use a two-domain nested setup in WRF-LES-GAD with grid spacings of 300 and 20 m. Both domains use an LES closure. The nested grids are forced by the 3 km HRRRv4 model, which best captures the MCS by assimilating NEXRAD data. In this setup, the 300 m domain serves as the MCS-resolving grid, while the 20 m domain resolves ambient, small-scale turbulence as well as wake-generated turbulence. The effect of 50 wind turbines representing the eastern half of the King Plains wind farm are included on the 20 m domain using a generalized actuator disk approach.

The bore formation and propagation and ultimately the structure of the gravity waves traveling through the AWAKEN region were found to be highly sensitive to the microphysics parameterization, as found in previous work (Johnson et al., 2018). We investigated three different microphysics schemes: the Thompson parameterization (1.5-moment scheme), the WRF 6-class (WDM6) parameterization (double-moment scheme), and the Morrison parameterization (double-moment scheme). Simulations with the WDM6 parameterization provided results with waves separated by 5 min, which best matched observations from lidars. The WDM6 scheme produces a more realistic bore structure, because the rain water mixing ratio profile shows a strong decrease below the cloud base, compared to relatively constant profiles for Thompson and Morrison. The decrease in rain water mixing ratio results in more latent cooling and thus a stronger cold pool and density current. Additionally, the Thompson and Morrison parameterizations result in more snow and less graupel and rain at higher altitudes. These results align with those of Johnson et al. (2018), who hypothesized that the increase in snow hydrometeors results in lower fall velocities in comparison to rain drops and thus less precipitation.

For the fine-scale domain with 20 m horizontal grid spacing and the wind turbines parameterized, the ambient turbulence was sensitive to the LES closure. Considering that 20 m is relatively coarse for a SBL simulation, resolving ambient

turbulence is a challenge for conventional closure schemes. While using finer grid resolution would be desirable, considering the large geographic extent of the region, 20 m grid spacing represented a compromise to reduce computational cost while still providing acceptable modeling results. For the given setup and case study, results with dynamic turbulence closures are more effective at capturing small-scale turbulence. This agrees with previous work that has shown that dynamic turbulence closures are more effective in SBL conditions and at coarser grid resolutions compared to conventional closures (Zhou and Chow, 2011, 2012, 2014; Wise, 2024a).

The bore passage and associated gravity waves generated by the MCS affect both the average power production and the power variability during the study period. Prior to the bore event, the wind turbines experienced an easterly low-level jet (LLJ), but the passage of the bore and gravity waves modulated the mesoscale environment substantially. After the gravity wave passage, the LLJ is effectively destroyed, with a much weaker jet nose resulting in reduced hub-height wind speeds, as was seen in both observations and modeling results. The LLJ is weakened because the gravity waves increase the SBL height, which is a common characteristic of bore events. As a result, the average power production decreases after the gravity wave passes, by up to 56 % depending on the turbine row and 39 % on average for all four rows. During the gravity wave passage, the power variability is increased by over 100 % for the most southern row of turbines. Similar trends were observed in wind turbine SCADA data. The increase in power variability is shown to result from wind direction oscillations associated with the gravity wave passage with wind variability related to wave-induced turbulence also playing a role. The easterly wind direction is sub-optimal for the King Plains wind farm since the east–west layout was designed for a predominantly southerly wind direction.

The WRF-LES-GAD modeling setup presented here provides a framework for simulating atmospheric bore and gravity wave effects on a wind farm. This case study shows good agreement between model results and available observations, demonstrating the efficacy of this approach for understanding the interaction between realistic gravity waves and wind farms. Gravity waves are a common feature in the southern Great Plains, coming from many directions and with various amplitudes and periods. The modeling framework used here is well suited for other gravity wave case studies from the AWAKEN field campaign. Future work will focus on characterizing the different types of gravity wave events observed during AWAKEN to better understand their formation mechanisms and their effects on wind farm power production.

## Appendix A: Ambient turbulence sensitivity to closure scheme

For the AWAKEN model setup in the region surrounding the King Plains wind farm, domain d01 resolves the mesoscale bore and gravity waves, and the nested domain d02 additionally resolves smaller-scale ambient turbulence. At 20 m grid spacing and in stably stratified conditions, the role of the turbulence closure in representing ambient turbulence is critical, especially to accurately represent the dissipation of individual wind turbine wakes. While results using the DRM closure are used in the main text of this study, domain d02 is also run with the turbulent kinetic energy 1.5-order model (TKE-1.5) (Deardorff, 1980) and the Dynamic Wong–Lilly (DWL) model (Wong and Lilly, 1994) for comparison. The TKE-1.5 model (Deardorff, 1980) is one of the standard turbulence closures used in WRF (and many other LES modeling tools). This model solves a prognostic turbulent kinetic energy (TKE) equation, which describes the evolution of TKE and parameterizes sources and sinks from shear production, buoyancy production or suppression, turbulent mixing, and dissipation. The Dynamic Wong–Lilly (DWL) model is the subgrid-scale component of the DRM model (the DRM model uses a combination of the DWL eddy-viscosity model and the scale-similar RSFS term to create a mixed model for turbulence), with the DWL model using the explicit filter to dynamically solve for the eddy viscosity coefficients of interest (Lilly, 1992).

Figure A1 shows an instantaneous plan slice of hub-height wind speed at 06:00 UTC (prior to the gravity wave and after 1 h of spin up). Qualitatively, the wind speeds are very similar across all three closures; however, the fine-scale structure of turbulence is different. The wind direction is east-northeasterly, and wakes are seen as the slower wind speeds downwind of each individual turbine. For the TKE-1.5 closure, there are patches in the flow where there is very little turbulence, especially in the inflow regions upwind of the farm. Figure A2 highlights an inflow region in Fig. A1, with Fig. A2 showing both the wind speed and the vertical velocity where the qualitative differences in the wind speed and vertical velocity variance are more clear between the TKE-1.5 closure and the dynamic closures. In general, for the DWL and DRM closures, the small-scale wind speed variability is more uniform, which is more realistic for ambient turbulence.

High-quality hub-height turbulence observations are limited in the AWAKEN region; however, wind speeds in the rotor layer were measured at relatively high temporal frequency ( $\sim 0.25$  Hz) by the profiling Doppler lidar at Site A1. The lidar at A1 was a pulsed lidar, which allowed for this faster scan frequency. Using these measurements, the power spectra for the hub-height wind speed can be generated in time from 06:00 to 06:25 UTC (prior to the gravity waves), shown in Fig. A3, which can be directly compared with simulation results at A1. Note that the 16 min delay in which

the gravity waves arrive in the model has been accounted for, with the time period for the lidar in Fig. A3a and b being shifted to 05:44–06:09 UTC. The spectra are computed using Welch's method (Welch, 1967). Overall, there is reasonable agreement between the modeling results and measurements with limitations related to the relatively coarse grid resolution. The modeling results and measurements agree well in the inertial subrange and follow a slope of  $-5/3$  for part of the spectrum (Kolmogorov, 1941); however, the larger-scale or lower-frequency structures are overestimated, and the smaller-scale or higher-frequency structures are underestimated by the model.

The dynamic closures contain more energy at higher frequencies compared to TKE-1.5, as expected, with the DRM simulation containing the most energy in a frequency range of 0.012–0.016 Hz ( $\sim 60$ – $80$  s) compared to the other closures. At higher frequencies (above  $\sim 0.02$  Hz), the reduction in energy due to the effect of the grid cutoff is apparent, as is typical for finite difference schemes (Skamarock, 2004). Additionally, because the high-frequency turbulence is underestimated, the energy content is shifted to lower frequencies, which results in an overestimation of larger-scale turbulence in the model compared to observations. A similar shift occurred in SBL conditions for Wise et al. (2022) and in neutral boundary layer conditions for Wiersema et al. (2022), and this is indicative of large-scale structures not cascading into smaller-scale motions limited by the grid resolution. Importantly, the hub-height wind speed and turbulence intensity are well predicted by the model during the analysis period. For all three closures, the hub-height wind speed biases are under  $0.4 \text{ m s}^{-1}$ , and the mean absolute errors are less than  $1.0 \text{ m s}^{-1}$ . For the DRM closure, which we conclude to perform best in the spectral analysis, the model-predicted mean hub-height wind speed is  $4.50 \text{ m s}^{-1}$  compared to an observed wind speed of  $4.24 \text{ m s}^{-1}$  (the low values are because Site A1 is waked during the analysis period). Additionally, the mean model-predicted turbulence intensity is 17.9 % compared to an observed 16.5 % during 06:00 to 06:25 UTC.

To quantify the spatial variation in turbulence between the three closures, we use energy spectra in the vertical velocity signal along various east–west transects in domain d02. Figure A4 shows spectra in wave space of the vertical velocity for the three different closures taken along east–west transects that intersect Sites H, A1, and A2. Hereinafter, these transects will be denoted as Transect H, Transect A1, and Transect A2. The spectra are obtained following the methods of Durran et al. (2017) and Connolly et al. (2021) and consist of 650 points along the transect (excluding five points near the eastern and western boundaries). The spectra shown in Fig. A4 are an average of the individual spectra calculated at each output time step (every 15 s) from 06:00 to 06:25 UTC, prior to the gravity wave interaction. Transect H can be considered purely inflow, while the flow at other transects is affected by wind turbine wakes. Along Transect H (Fig. A4a), there is increased energy for larger wave numbers (smaller

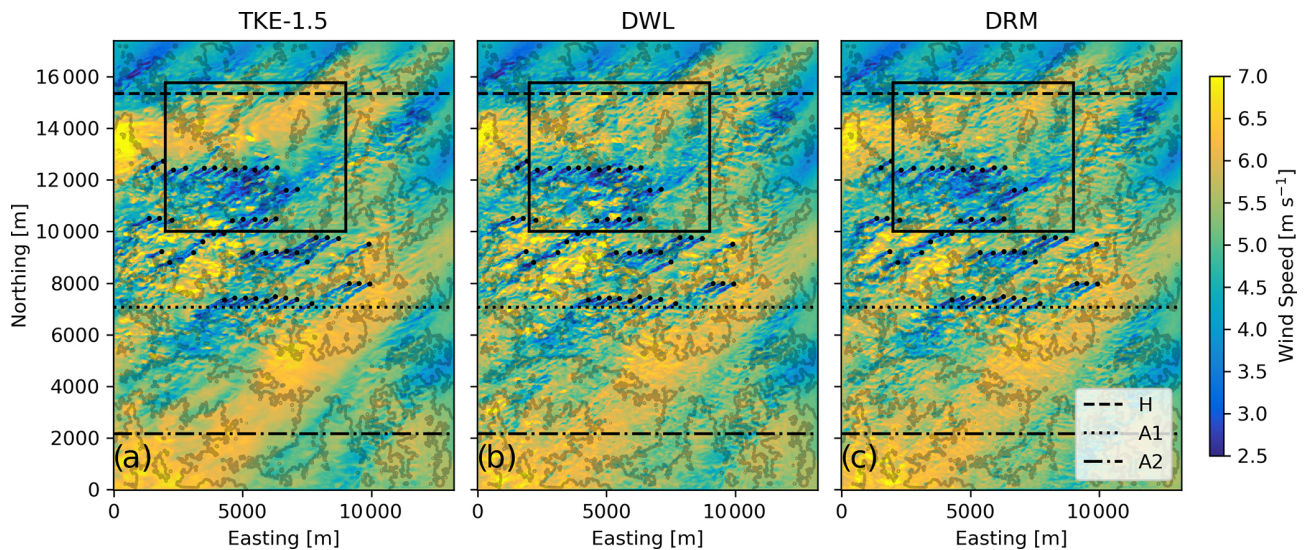


**Figure A1.** Plan slice of hub-height wind speed at 06:00 UTC in domain d02 for simulation results using the (a) TKE-1.5, (b) DWL, and (c) DRM turbulence closures. The area outlined in black is the extent shown in Fig. A2. Line contours represent 15 m changes in elevation.

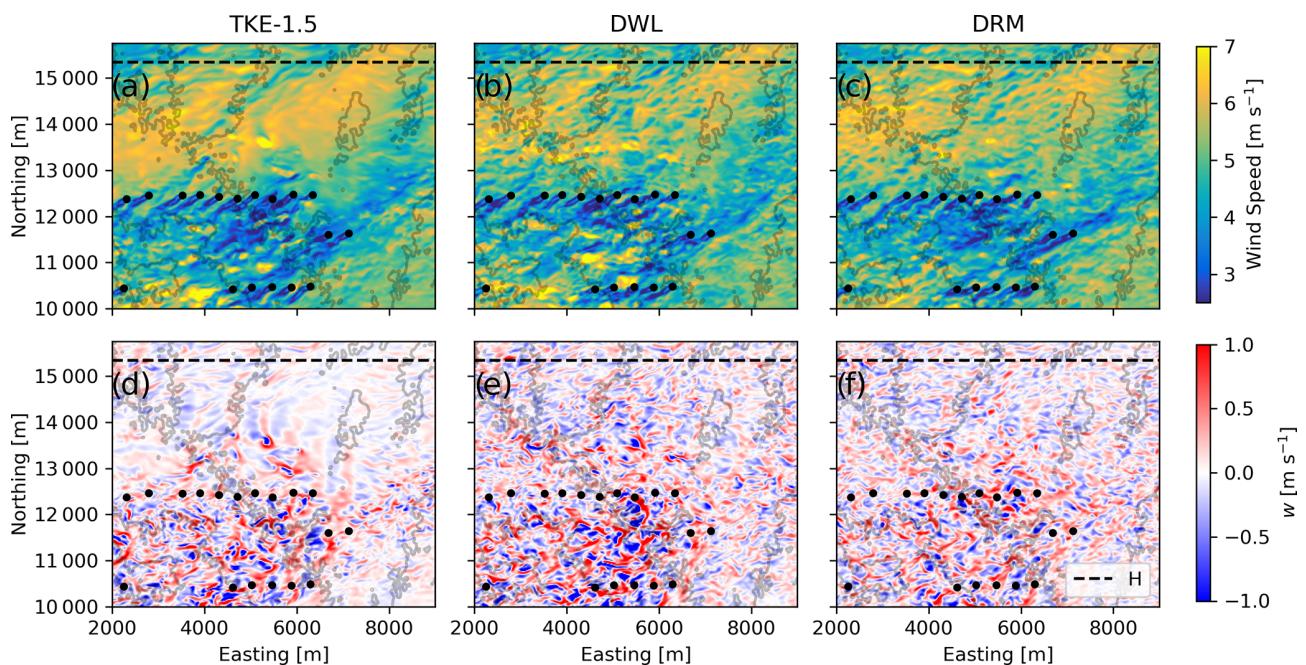


**Figure A2.** Zoomed-in plan slice of hub-height (a–c) wind speed and (d–f) vertical velocity at 06:00 UTC in domain d02 for simulations. Line contours represent 15 m changes in elevation.

wavelengths) when using the DWL and DRM closure compared to TKE-1.5, indicating that turbulence is more evenly distributed for the DWL and DRM closures. A similar trend holds true for Transects A1 and A2 (Fig. A4b and c) but to a much lower degree. Additionally, Transects A1 and A2 contain more energy in the smaller scales, as these locations are downstream of the wind farm and therefore contain added energy from wind turbine wake turbulence.

Ultimately, the DRM closure was used for further analysis as it best represents the ambient turbulent structures and provides good agreement for the hub-height wind speed and turbulence intensity. There has been significant research on the sensitivity of LES modeling results in SBL conditions to the turbulence closure, and the present work agrees with previous findings in that dynamic turbulence models are able to resolve more turbulence in stably stratified conditions (Zhou and Chow, 2011, 2012, 2014; Wise, 2024a). Interestingly,

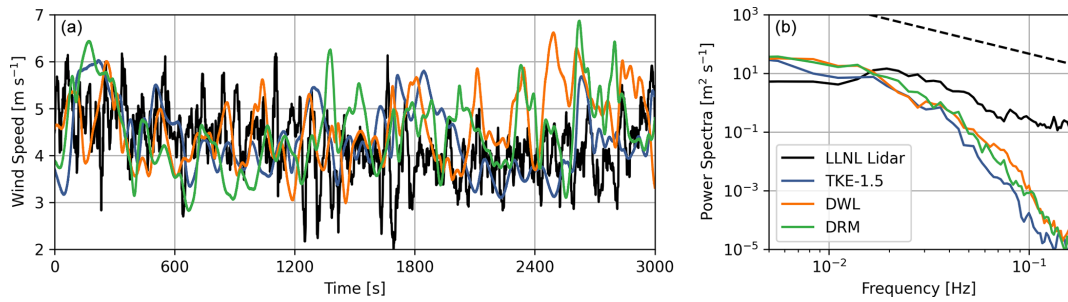


**Figure A3.** Time series (a) and power spectral density (b) of wind speed at Site A1 for the observations and simulation results with the various closures prior to the gravity waves. The analysis period for the modeling results is 06:00–06:25 and 05:44–06:09 UTC to account for the delay in which the gravity waves occur in the model. The dashed black line in (b) represents the  $-5/3$  energy cascade range in the inertial subrange.

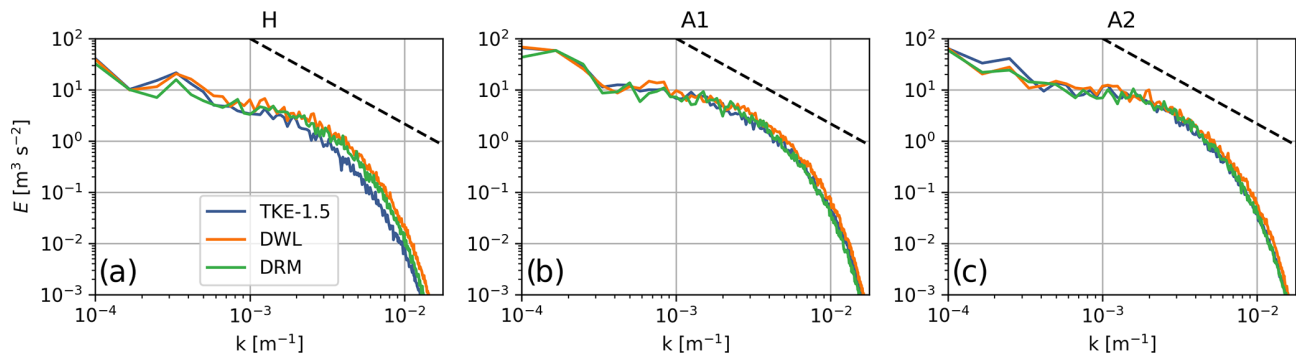


**Figure A4.** Wave-space spectra of vertical velocity for the various closures along the (a) H, (b) E, and (c) A1 east–west transects. Spectra are calculated every 15 s from 06:00 to 06:25 UTC and then averaged. The dashed black line represents the  $-5/3$  energy cascade range in the inertial subrange.

other simulations of the same site at the same grid resolution but focusing on shear-driven instabilities in strong SBL conditions showed dramatic differences in the quality of ambient turbulence to the closure (see Appendix E in Wise, 2024a). In contrast with the study of Wise (2024a), the current setup takes advantage of HRRRv4 forcing and the CPM, which is one reason why there are smaller differences in the representation of turbulence when using the different closures in this study. Another likely reason is that the strength of stratification is weaker in the present study compared to Wise (2024a).

**Code and data availability.** The full WRF-LES-GAD simulation data are several terabytes, but subsets of the data can be shared upon request. The source code can be found at <https://doi.org/10.5281/zenodo.15492528> (Wise, 2025). All the data are publicly available on the ARM Discovery web page (<https://doi.org/10.5439/1890922>, Newsom and Krishnamurthy, 2024) or on the Wind Data Hub (<https://www.a2e.energy.gov>, U.S. Department of Energy, 2024). The ARM lidar data DOI at site A1 is <https://doi.org/10.2172/1034640> (Newsom and Krishnamurthy, 2022), and the LLNL lidar data DOI at site A1 is <https://doi.org/10.21947/2516855> (Wharton, 2023).

**Video supplement.** The following animations are available online at <https://doi.org/10.5281/zenodo.12551368> (Wise, 2024b): Video 1 is the NEXRAD WSR-88D radar reflectivity over central Oklahoma from 03:30 to 06:00 UTC on 6 June 2023; Video 2 is the wind speeds from TTU X-band radars at heights of 95, 145, and 270 m a.g.l. from 05:30–07:30 UTC; Video 3 is the simulated vertical velocity at 1 km a.g.l. and potential temperature at 200 m a.g.l. on domain d01 ( $\Delta x = 300$  m); and Video 4 is the simulated hub-height wind speed, perturbation pressure, and turbine power output on domain d02 ( $\Delta x = 20$  m).

**Author contributions.** Writing (original draft preparation) and visualization: ASW. Writing (review and editing): RSA, AA, SW, RK, RN, BH, JS, PM, and FKC. Methodology, software, validation, and formal analysis: ASW, RSA, AA, and FKC. Conceptualization: ASW, RSA, PM, and FKC. Investigation and data curation: AA, SW, RK, RN, BH, and JS. All authors contributed with critical feedback on this research and have read and agreed to the published version of the paper.

**Competing interests.** The contact author has declared that none of the authors has any competing interests.

**Disclaimer.** The views expressed in the article do not necessarily represent the views of the DOE or the U.S. Government.

**Publisher's note:** Copernicus Publications remains neutral with regard to jurisdictional claims made in the text, published maps, institutional affiliations, or any other geographical representation in this paper. While Copernicus Publications makes every effort to include appropriate place names, the final responsibility lies with the authors.

**Acknowledgements.** Correspondence with Aaron Johnson of the University of Oklahoma regarding bore modeling in WRF was greatly appreciated. This research used the Savio computational cluster resource provided by the Berkeley Research Computing program at the University of California, Berkeley (supported by the UC Berkeley Chancellor, Vice Chancellor for Research, and Chief Information Officer). Robert S. Arthur's and Sonia Wharton's contributions were prepared by Lawrence Livermore National Laboratory under contract DE-AC52-07NA27344, with support from the US DOE Office of Energy Efficiency and Renewable Energy Wind Energy Technologies Office. Pacific Northwest National Laboratory is operated for DOE by the Battelle Memorial Institute under contract DE-AC05-76RLO1830. This work was authored (in part) by the National Renewable Energy Laboratory, operated by Alliance for Sustainable Energy, LLC, for the US Department of Energy (DOE) under contract no. DE-AC36-08GO28308. Funding provided by the US Department of Energy Office of Energy Efficiency and Renewable Energy Wind Energy Technologies Office.

**Financial support.** This research has been supported by the US Department of Energy purchase order with Sandia National Laboratories and the National Science Foundation Graduate Research Fellowship Program (grant no. 1752814).

**Review statement.** This paper was edited by Sukanta Basu and reviewed by three anonymous referees.

## References

- Aitken, M. L., Kosović, B., Mirocha, J. D., and Lundquist, J. K.: Large eddy simulation of wind turbine wake dynamics in the stable boundary layer using the Weather Research and Forecasting Model, *J. Renew. Sustain. Ener.*, 6, 033137, <https://doi.org/10.1063/1.4885111>, 2014.
- Allaerts, D. and Meyers, J.: Gravity Waves and Wind-Farm Efficiency in Neutral and Stable Conditions, *Bound.-Lay. Meteorol.*, 166, 269–299, <https://doi.org/10.1007/s10546-017-0307-5>, 2018.
- Arthur, R. S., Mirocha, J. D., Marjanovic, N., Hirth, B. D., Schroeder, J. L., Wharton, S., and Chow, F. K.: Multi-Scale Simulation of Wind Farm Performance during a Frontal Passage, *Atmosphere*, 11, 245, <https://doi.org/10.3390/atmos11030245>, 2020.
- Blaylock, B. K., Horel, J. D., and Crosman, E. T.: Impact of Lake Breezes on Summer Ozone Concentrations in the Salt Lake Valley, *J. Appl. Meteorol. Climatol.*, 56, 353–370, <https://doi.org/10.1175/JAMC-D-16-0216.1>, 2017.
- Carbajo Fuertes, F., Markfort, C. D., and Porté-Agel, F.: Wind Turbine Wake Characterization with Nacelle-Mounted Wind Lidars for Analytical Wake Model Validation, *Remote Sens.*, 10, 668, <https://doi.org/10.3390/rs10050668>, 2018.
- Chen, B., Thompson, T., and Chow, F. K.: Hyper-local source strength retrieval and apportionment of black carbon in an urban area, *Atmos. Environ.*, 22, 100252, <https://doi.org/10.1016/j.aeoa.2024.100252>, 2024.
- Chen, F. and Dudhia, J.: Coupling an advanced land surface-hydrology model with the Penn State-NCAR MM5 modeling system. Part I: Model implementation and sensitivity, *Mon. Weather Rev.*, 129, 569–585, 2001.
- Chow, F., Schär, C., Ban, N., Lundquist, K., Schlemmer, L., and Shi, X.: Crossing Multiple Gray Zones in the Transition from Mesoscale to Microscale Simulation over Complex Terrain, *Atmosphere*, 10, 274, <https://doi.org/10.3390/atmos10050274>, 2019.
- Chow, F. K.: Subfilter-scale turbulence modeling for large-eddy simulation of the atmospheric boundary layer over complex terrain, Ph.D. dissertation, Stanford University, 2004.
- Chow, F. K., Street, R. L., Xue, M., and Ferziger, J. H.: Explicit Filtering and Reconstruction Turbulence Modeling for Large-Eddy Simulation of Neutral Boundary Layer Flow, *J. Atmos. Sci.*, 62, 2058–2077, <https://doi.org/10.1175/JAS3456.1>, 2005.
- Connolly, A., van Veen, L., Neher, J., Geurts, B. J., Mirocha, J., and Chow, F. K.: Efficacy of the Cell Perturbation Method in Large-Eddy Simulations of Boundary Layer Flow over Complex Terrain, *Atmosphere*, 12, 55, <https://doi.org/10.3390/atmos12010055>, 2021.
- Cook, D. R.: Eddy Correlation Flux Measurement System (ECOR) Instrument Handbook, <https://doi.org/10.2172/1467448>, 2018.
- Deardorff, J. W.: Stratocumulus-capped mixed layers derived from a three-dimensional model, *Bound.-Lay. Meteorol.*, 18, 495–527, 1980.
- Debnath, M., Scholbrock, A. K., Zalkind, D., Moriarty, P., Simley, E., Hamilton, N., Ivanov, C., Arthur, R. S., Barthelmie, R., Bordini, N., Brewer, A., Goldberger, L., Herges, T., Hirth, B., Valerio Iungo, G., Jager, D., Kaul, C., Klein, P., Krishnamurthy, R., Letizia, S., Lundquist, J. K., Maniaci, D., Newsom, R., Pekour, M., Pryor, S. C., Ritsche, M. T., Roadman, J., Schroeder, J., Shaw, W. J., Van Dam, J., and Wharton, S.: Design of the American Wake Experiment (AWAKEN) field campaign, *J. Phys. Conf. Ser.*, 2265, 022058, <https://doi.org/10.1088/1742-6596/2265/2/022058>, 2022.
- Debnath, M., Moriarty, P., Krishnamurthy, R., Bordini, N., Newsom, R., Quon, E., Lundquist, J. K., Letizia, S., Iungo, G. V., and Klein, P.: Characterization of wind speed and directional shear at the AWAKEN field campaign site, *J. Renew. Sustain. Ener.*, 15, 033308, <https://doi.org/10.1063/5.0139737>, 2023.
- Dowell, D. C., Alexander, C. R., James, E. P., Weygandt, S. S., Benjamin, S. G., Manikin, G. S., Blake, B. T., Brown, J. M., Olson, J. B., Hu, M., Smirnova, T. G., Ladwig, T., Kenyon, J. S., Ahmadov, R., Turner, D. D., Duda, J. D., and Alcott, T. I.: The High-Resolution Rapid Refresh (HRRR): An Hourly Updating Convection-Allowing Forecast Model. Part I: Motivation and System Description, *Weather Forecast.*, 37, 1371–1395, <https://doi.org/10.1175/WAF-D-21-0151.1>, 2022.

- Dudhia, J.: Numerical study of convection observed during the winter monsoon experiment using a mesoscale two-dimensional model, *J. Atmos. Sci.*, 46, 3077–3107, 1989.
- Durran, D., Weyn, J. A., and Menchaca, M. Q.: Practical considerations for computing dimensional spectra from gridded data, *Mon. Weather Rev.*, 145, 3901–3910, 2017.
- Farr, T. G., Rosen, P. A., Caro, E., Crippen, R., Duren, R., Hensley, S., Kobrick, M., Paller, M., Rodriguez, E., Roth, L., Seal, D., Shaffer, S., Shimada, J., Umland, J., Werner, M., Oskin, M., Burbank, D., and Alsdorf, D.: The shuttle radar topography mission, *Rev. Geophys.*, 45, <https://doi.org/10.1029/2005RG000183>, 2007.
- Feng, Z., Houze, R. A., Leung, L. R., Song, F., Hardin, J. C., Wang, J., Gustafson, W. I., and Homeyer, C. R.: Spatiotemporal Characteristics and Large-Scale Environments of Mesoscale Convective Systems East of the Rocky Mountains, *J. Climate*, 32, 7303–7328, <https://doi.org/10.1175/JCLI-D-19-0137.1>, 2019.
- Geerts, B., Parsons, D., Ziegler, C. L., Weckwerth, T. M., Biggerstaff, M. I., Clark, R. D., Coniglio, M. C., Demoz, B. B., Ferrare, R. A., Gallus, W. A., Haghi, K., Hanesiak, J. M., Klein, P. M., Knupp, K. R., Kosiba, K., McFarquhar, G. M., Moore, J. A., Nehrir, A. R., Parker, M. D., Pinto, J. O., Rauber, R. M., Schumacher, R. S., Turner, D. D., Wang, Q., Wang, X., Wang, Z., and Wurman, J.: The 2015 Plains Elevated Convection at Night Field Project, *B. Am. Meteorol. Soc.*, 98, 767–786, <https://doi.org/10.1175/BAMS-D-15-00257.1>, 2017.
- Germano, M., Piomelli, U., Moin, P., and Cabot, W. H.: A dynamic subgrid-scale eddy viscosity model, *Phys. Fluids A*, 3, 1760–1765, <https://doi.org/10.1063/1.857955>, 1991.
- Haghi, K. R. and Durran, D. R.: On the Dynamics of Atmospheric Bores, *J. Atmos. Sci.*, 78, 313–327, <https://doi.org/10.1175/JAS-D-20-0181.1>, 2021.
- Haghi, K. R., Parsons, D. B., and Shapiro, A.: Bores Observed during IHOP\_2002: The Relationship of Bores to the Nocturnal Environment, *Mon. Weather Rev.*, 145, 3929–3946, <https://doi.org/10.1175/MWR-D-16-0415.1>, 2017.
- Haghi, K. R., Geerts, B., Chipilski, H. G., Johnson, A., Degelia, S., Imy, D., Parsons, D. B., Adams-Selin, R. D., Turner, D. D., and Wang, X.: Bore-ing into Nocturnal Convection, *B. Am. Meteorol. Soc.*, 100, 1103–1121, <https://doi.org/10.1175/BAMS-D-17-0250.1>, 2019.
- Han, B., Fan, J., Varble, A., Morrison, H., Williams, C. R., Chen, B., Dong, X., Giangrande, S. E., Khain, A., Mansell, E., Milbrandt, J. A., Shpund, J., and Thompson, G.: Cloud-Resolving Model Intercomparison of an MC3E Squall Line Case: Part II. Stratiform Precipitation Properties, *J. Geophys. Res.-Atmos.*, 124, 1090–1117, <https://doi.org/10.1029/2018JD029596>, 2019.
- Haupt, S. E., Kosović, B., Shaw, W., Berg, L. K., Churchfield, M., Cline, J., Draxl, C., Ennis, B., Koo, E., Kotamarthi, R., Mazzaro, L., Mirocha, J., Moriarty, P., Muñoz-Esparza, D., Quon, E., Rai, R. K., Robinson, M., and Sever, G.: On Bridging a Modeling Scale Gap: Mesoscale to Microscale Coupling for Wind Energy, *B. Am. Meteorol. Soc.*, 100, 2533–2550, <https://doi.org/10.1175/BAMS-D-18-0033.1>, 2019.
- Hersbach, H., Bell, B., Berrisford, P., Hirahara, S., Horányi, A., Muñoz-Sabater, J., Nicolas, J., Peubey, C., Radu, R., Schepers, D., Simmons, A., Soci, C., Abdalla, S., Abellan, X., Balsamo, G., Bechtold, P., Biavati, G., Bidlot, J., Bonavita, M., De Chiara, G., Dahlgren, P., Dee, D., Diamantakis, M., Dragani, R., Flemming, J., Forbes, R., Fuentes, M., Geer, A., Haimberger, L., Healy, S., Hogan, R. J., Hólm, E., Janisková, M., Keeley, S., Laloyaux, P., Lopez, P., Lupu, C., Radnoti, G., de Rosnay, P., Rozum, I., Vamborg, F., Villaume, S., and Thépaut, J.-N.: The ERA5 global reanalysis, *Q. J. Roy. Meteor. Soc.*, 146, 1999–2049, <https://doi.org/10.1002/qj.3803>, 2020.
- Hirth, B. D., Schroeder, J. L., and Guynes, J. G.: Diurnal evolution of wind structure and data availability measured by the DOE prototype radar system, *J. Phys. Conf. Ser.*, 926, 012003, <https://doi.org/10.1088/1742-6596/926/1/012003>, 2017.
- Hirth, B. D., Schroeder, J. L., and Guynes, J. G.: An On-shore Deployment of Advanced Dual-Doppler Radar for Wind Energy Applications, *J. Phys. Conf. Ser.*, 2745, 012013, <https://doi.org/10.1088/1742-6596/2745/1/012013>, 2024.
- Houze Jr., R. A.: Mesoscale convective systems, *Rev. Geophys.*, 42, RG2004, <https://doi.org/10.1029/2004RG000150>, 2004.
- Janjić, Z. I.: The step-mountain eta coordinate model: Further developments of the convection, viscous sublayer, and turbulence closure schemes, *Mon. Weather Rev.*, 122, 927–945, 1994.
- Johnson, A. and Wang, X.: Design and Implementation of a GSI-Based Convection-Allowing Ensemble Data Assimilation and Forecast System for the PECAN Field Experiment. Part I: Optimal Configurations for Nocturnal Convection Prediction Using Retrospective Cases, *Weather Forecast.*, 32, 289–315, <https://doi.org/10.1175/WAF-D-16-0102.1>, 2017.
- Johnson, A. and Wang, X.: Multicase Assessment of the Impacts of Horizontal and Vertical Grid Spacing, and Turbulence Closure Model, on Subkilometer-Scale Simulations of Atmospheric Bores during PECAN, *Mon. Weather Rev.*, 147, 1533–1555, <https://doi.org/10.1175/MWR-D-18-0322.1>, 2019.
- Johnson, A., Wang, X., and Degelia, S.: Design and Implementation of a GSI-Based Convection-Allowing Ensemble-Based Data Assimilation and Forecast System for the PECAN Field Experiment. Part II: Overview and Evaluation of a Real-Time System, *Weather Forecast.*, 32, 1227–1251, <https://doi.org/10.1175/WAF-D-16-0201.1>, 2017.
- Johnson, A., Wang, X., Haghi, K. R., and Parsons, D. B.: Evaluation of Forecasts of a Convectively Generated Bore Using an Intensively Observed Case Study from PECAN, *Mon. Weather Rev.*, 146, 3097–3122, <https://doi.org/10.1175/MWR-D-18-0059.1>, 2018.
- Keane, A., Aguirre, P. E. O., Ferchland, H., Clive, P., and Gallacher, D.: An analytical model for a full wind turbine wake, *J. Phys. Conf. Ser.*, 753, 032039, <https://doi.org/10.1088/1742-6596/753/3/032039>, 2016.
- Kirkil, G., Mirocha, J., Bou-Zeid, E., Chow, F. K., and Kosović, B.: Implementation and Evaluation of Dynamic Subfilter-Scale Stress Models for Large-Eddy Simulation Using WRF\*, *Mon. Weather Rev.*, 140, 266–284, <https://doi.org/10.1175/MWR-D-11-00037.1>, 2012.
- Knupp, K.: Observational Analysis of a Gust Front to Bore to Solitary Wave Transition within an Evolving Nocturnal Boundary Layer, *J. Atmos. Sci.*, 63, 2016–2035, <https://doi.org/10.1175/JAS3731.1>, 2006.
- Kolmogorov, A. N.: The Local Structure of Turbulence in Incompressible Viscous Fluid for Very Large Reynolds' Numbers, in: *Dokl. Akad. Nauk SSSR*, 30, 301–305, 1941.
- Krishnamurthy, R., Newsom, R. K., Chand, D., and Shaw, W. J.: Boundary Layer Climatology at ARM Southern Great Plains,

- U.S. Department of Energy, <https://doi.org/10.2172/1779279>, 2021.
- Krishnamurthy, R., Newsom, R. K., Kaul, C. M., Letizia, S., Pekour, M., Hamilton, N., Chand, D., Flynn, D., Bodini, N., and Moriarty, P.: Observations of wind farm wake recovery at an operating wind farm, *Wind Energ. Sci.*, 10, 361–380, <https://doi.org/10.5194/wes-10-361-2025>, 2025.
- Lanzilao, L. and Meyers, J.: Effects of self-induced gravity waves on finite wind-farm operations using a large-eddy simulation framework, *J. Phys. Conf. Ser.*, 2265, 022043, <https://doi.org/10.1088/1742-6596/2265/2/022043>, 2022.
- Lilly, D. K.: A proposed modification of the Germano sub-grid-scale closure method, *Phys. Fluids A*, 4, 633–635, <https://doi.org/10.1063/1.858280>, 1992.
- Lim, K.-S. S. and Hong, S.-Y.: Development of an Effective Double-Moment Cloud Microphysics Scheme with Prognostic Cloud Condensation Nuclei (CCN) for Weather and Climate Models, *Mon. Weather Rev.*, 138, 1587–1612, <https://doi.org/10.1175/2009MWR2968.1>, 2010.
- Lundquist, J. K.: Intermittent and Elliptical Inertial Oscillations in the Atmospheric Boundary Layer, *J. Atmos. Sci.*, 60, 2661–2673, [https://doi.org/10.1175/1520-0469\(2003\)060<2661:IAEIOI>2.0.CO;2](https://doi.org/10.1175/1520-0469(2003)060<2661:IAEIOI>2.0.CO;2), 2003.
- Markowski, P. and Richardson, Y.: *Mesoscale Convective Systems*, Chap. 9, 245–272, John Wiley & Sons, Ltd, ISBN 9780470682104, <https://doi.org/10.1002/9780470682104.ch9>, 2010.
- Mazzaro, L. J., Muñoz-Esparza, D., Lundquist, J. K., and Linn, R. R.: Nested mesoscale-to-LES modeling of the atmospheric boundary layer in the presence of under-resolved convective structures, *J. Adv. Model. Earth Sy.*, 9, 1795–1810, <https://doi.org/10.1002/2017MS000912>, 2017.
- Mirocha, J. D., Kosović, B., Aitken, M. L., and Lundquist, J. K.: Implementation of a generalized actuator disk wind turbine model into the weather research and forecasting model for large-eddy simulation applications, *J. Renew. Sustain. Ener.*, 6, 013104, <https://doi.org/10.1063/1.4861061>, 2014.
- Mlawer, E. J., Taubman, S. J., Brown, P. D., Iacono, M. J., and Clough, S. A.: Radiative transfer for inhomogeneous atmospheres: RRTM, a validated correlated-k model for the longwave, *J. Geophys. Res.-Atmos.*, 102, 16663–16682, 1997.
- Monin, A. S. and Obukhov, A. M.: Basic laws of turbulent mixing in the surface layer of the atmosphere, *Contrib. Geophys. Inst. Acad. Sci. USSR*, 151, e187, 1954.
- Moriarty, P., Hamilton, N., Debnath, M., Herges, T., Isom, B., Lundquist, J., Maniaci, D., Naughton, B., Pauly, R., Roadman, J., Shaw, W., Van Dam, J., and Wharton, S.: American WAKE experimeNt (AWAKEN), Tech. Rep. NREL/TP-5000-75789, 1659798, MainId:5894, <https://doi.org/10.2172/1659798>, 2020.
- Moriarty, P., Bodini, N., Letizia, S., Abraham, A., Ashley, T., Bärfuss, K. B., Barthelmie, R. J., Brewer, A., Brugger, P., Feuerle, T., Frère, A., Goldberger, L., Gottschall, J., Hamilton, N., Herges, T., Hirth, B., Hung, L.-Y., Iungo, G. V., Ivanov, H., Kaul, C., Kern, S., Klein, P., Krishnamurthy, R., Lampert, A., Lundquist, J. K., Morris, V. R., Newsom, R., Pekour, M., Pichugina, Y., Porté-Angel, F., Pryor, S. C., Scholbrock, A., Schroeder, J., Shartzer, S., Simley, E., Vöhringer, L., Wharton, S., Zalkind, D.: Overview of preparation for the American WAKE ExperimeNt (AWAKEN), *J. Renew. Sustain. Ener.*, 16, 053306, <https://doi.org/10.1063/5.0141683>, 2024.
- Morrison, H., Thompson, G., and Tatarskii, V.: Impact of Cloud Microphysics on the Development of Trailing Stratiform Precipitation in a Simulated Squall Line: Comparison of One- and Two-Moment Schemes, *Mon. Weather Rev.*, 137, 991–1007, <https://doi.org/10.1175/2008MWR2556.1>, 2009.
- Morrison, H., van Lier-Walqui, M., Fridlind, A. M., Grabowski, W. W., Harrington, J. Y., Hoose, C., Korolev, A., Kumjian, M. R., Milbrandt, J. A., Pawlowska, H., Posselt, D. J., Prat, O. P., Reimel, K. J., Shima, S.-I., van Dierenhoven, B., and Xue, L.: Confronting the Challenge of Modeling Cloud and Precipitation Microphysics, *J. Adv. Model. Earth Sy.*, 12, e2019MS001689, <https://doi.org/10.1029/2019MS001689>, 2020.
- Muller, C. and Abramian, S.: The cloud dynamics of convective storm systems, *Physics Today*, 76, 28–28, <https://doi.org/10.1063/PT.3.5234>, 2023.
- Muñoz-Esparza, D., Kosović, B., Mirocha, J., and van Beeck, J.: Bridging the transition from mesoscale to microscale turbulence in numerical weather prediction models, *Bound.-Lay. Meteorol.*, 153, 409–440, 2014.
- Muñoz-Esparza, D., Kosović, B., Van Beeck, J., and Mirocha, J.: A stochastic perturbation method to generate inflow turbulence in large-eddy simulation models: Application to neutrally stratified atmospheric boundary layers, *Phys. Fluids*, 27, 035102, <https://doi.org/10.1063/1.4913572>, 2015.
- Muñoz-Esparza, D., Lundquist, J. K., Sauer, J. A., Kosović, B., and Linn, R. R.: Coupled mesoscale-LES modeling of a diurnal cycle during the CWEX-13 field campaign: From weather to boundary-layer eddies, *J. Adv. Model. Earth Sy.*, 9, 1572–1594, <https://doi.org/10.1002/2017MS000960>, 2017.
- National Centers for Environmental Prediction, National Weather Service, NOAA, U.S. Department of Commerce: NCEP GFS 0.25 Degree Global Forecast Grids Historical Archive, <https://doi.org/10.5065/D65D8PWK>, 2015.
- Newsom, R. and Krishnamurthy, R.: Doppler Lidar (DL) Instrument Handbook, U.S. Department of Energy [data set], <https://doi.org/10.2172/1034640>, 2022.
- Newsom, R. and Krishnamurthy, R.: Doppler Lidar (DLPII2) Site A1 (S4) for AWAKEN, ARM Data Discovery [data set], <https://doi.org/10.5439/1890922>, 2024.
- Newsom, R. K. and Banta, R. M.: Shear-Flow Instability in the Stable Nocturnal Boundary Layer as Observed by Doppler Lidar during CASES-99, *J. Atmos. Sci.*, 60, 16–33, [https://doi.org/10.1175/1520-0469\(2003\)060<0016:SFIIITS>2.0.CO;2](https://doi.org/10.1175/1520-0469(2003)060<0016:SFIIITS>2.0.CO;2), 2003.
- Olson, J. B., Kenyon, J. S., Angevine, W. A., Brown, J. M., Pagowski, M., and Sušelj, K.: A Description of the MYNN-EDMF Scheme and the Coupling to Other Components in WRF-ARW, NOAA Technical Memorandum OAR GSD, 61, <https://doi.org/10.25923/n9wm-be49>, 2019.
- Pandey, A., Lamraoui, F., Smith, J. B., Clapp, C. E., Sayres, D. S., and Kuang, Z.: Sensitivity of Deep Convection and Cross-Tropopause Water Transport to Microphysical Parameterizations in WRF, *J. Geophys. Res.-Atmos.*, 128, e2022JD037053, <https://doi.org/10.1029/2022JD037053>, 2023.
- Quon, E.: NREL/openfast-turbine-models, GitHub [code], <https://github.com/NREL/openfast-turbine-models/tree/main/IEA-scaled/NREL-2.8-127>, 2024.

- Ralph, F. M., Neiman, P. J., and Keller, T. L.: Deep-Tropospheric Gravity Waves Created by Leaside Cold Fronts, *J. Atmos. Sci.*, 56, 2986–3009, [https://doi.org/10.1175/1520-0469\(1999\)056<2986:DTGWCB>2.0.CO;2](https://doi.org/10.1175/1520-0469(1999)056<2986:DTGWCB>2.0.CO;2), 1999.
- Rottman, J. W. and Simpson, J. E.: The formation of internal bores in the atmosphere: A laboratory model, *Q. J. Roy. Meteor. Soc.*, 115, 941–963, <https://doi.org/10.1002/qj.49711548809>, 1989.
- Sanchez Gomez, M., Lundquist, J. K., Mirocha, J. D., Arthur, R. S., Muñoz-Esparza, D., and Robey, R.: Can lidars assess wind plant blockage in simple terrain? A WRF-LES study, *J. Renew. Sustain. Ener.*, 14, 063303, <https://doi.org/10.1063/5.0103668>, 2022.
- Sanchez Gomez, M., Lundquist, J. K., Mirocha, J. D., and Arthur, R. S.: Investigating the physical mechanisms that modify wind plant blockage in stable boundary layers, *Wind Energ. Sci.*, 8, 1049–1069, <https://doi.org/10.5194/wes-8-1049-2023>, 2023.
- Sathe, A., Mann, J., Vasiljevic, N., and Lea, G.: A six-beam method to measure turbulence statistics using ground-based wind lidars, *Atmos. Meas. Tech.*, 8, 729–740, <https://doi.org/10.5194/amt-8-729-2015>, 2015.
- Schreiber, J., Balbaa, A., and Bottasso, C. L.: Brief communication: A double-Gaussian wake model, *Wind Energ. Sci.*, 5, 237–244, <https://doi.org/10.5194/wes-5-237-2020>, 2020.
- Simpson, J.: *Gravity Currents in the Environment and the Laboratory*, Cambridge University Press, ISBN-10 9780521561099, ISBN-13 978-0521561099, 1997.
- Skamarock, W. C.: Evaluating mesoscale NWP models using kinetic energy spectra, *Mon. Weather Rev.*, 132, 3019–3032, 2004.
- Skamarock, W. C., Klemp, J. B., Dudhia, J., Gill, D. O., Liu, Z., Berner, J., Wang, W., Powers, J. G., Duda, M. G., Barker, D. M., and Huang, X.-Y.: A Description of the Advanced Research WRF Model Version 4, technical report, <https://doi.org/10.5065/1dfh-6p97>, 2021.
- Stipa, S., Ahmed Khan, M., Allaerts, D., and Brinkerhoff, J.: A large-eddy simulation (LES) model for wind-farm-induced atmospheric gravity wave effects inside conventionally neutral boundary layers, *Wind Energ. Sci.*, 9, 1647–1668, <https://doi.org/10.5194/wes-9-1647-2024>, 2024.
- Stull, R.: *An Introduction to Boundary Layer Meteorology, Atmospheric and Oceanographic Sciences Library*, Springer Netherlands, ISBN 9789027727695, 1988.
- Sun, J., Burns, S. P., Lenschow, D. H., Banta, R., Newsom, R., Coulter, R., Frasier, S., Ince, T., Nappo, C., Cuxart, J., Blumen, W., Lee, X., and Hu, X.-Z.: Intermittent Turbulence Associated with a Density Current Passage in the Stable Boundary Layer, *Bound.-Lay. Meteorol.*, 105, 199–219, <https://doi.org/10.1023/A:1019969131774>, 2002.
- Tatsuya Seiki, W. R. and Satoh, M.: Cloud Microphysics in Global Cloud Resolving Models, *Atmosphere-Ocean*, 60, 477–505, <https://doi.org/10.1080/07055900.2022.2075310>, 2022.
- Thompson, G., Field, P. R., Rasmussen, R. M., and Hall, W. D.: Explicit Forecasts of Winter Precipitation Using an Improved Bulk Microphysics Scheme. Part II: Implementation of a New Snow Parameterization, *Mon. Weather Rev.*, 136, 5095–5115, <https://doi.org/10.1175/2008MWR2387.1>, 2008.
- Tomaszewski, J. M. and Lundquist, J. K.: Observations and simulations of a wind farm modifying a thunderstorm outflow boundary, *Wind Energ. Sci.*, 6, 1–13, <https://doi.org/10.5194/wes-6-1-2021>, 2021.
- Toms, B. A., Tomaszewski, J. M., Turner, D. D., and Koch, S. E.: Analysis of a Lower-Tropospheric Gravity Wave Train Using Direct and Remote Sensing Measurement Systems, *Mon. Weather Rev.*, 145, 2791–2812, <https://doi.org/10.1175/MWR-D-16-0216.1>, 2017.
- U.S. Department of Energy: A2E Wind Data Hub, U.S. Department of Energy [data set], <https://www.a2e.energy.gov>, last access: 1 July 2024.
- U.S. Energy Information Administration: Oklahoma State Energy Profile, Tech. rep., Washington, D.C., <https://www.eia.gov/state/print.php?sid=OK> (last access: 1 July 2024), 2023.
- Vermeer, L., Sørensen, J., and Crespo, A.: Wind turbine wake aerodynamics, *Prog. Aerospace Sci.*, 39, 467–510, [https://doi.org/10.1016/S0376-0421\(03\)00078-2](https://doi.org/10.1016/S0376-0421(03)00078-2), 2003.
- Wang, J., Foley, S., Nanos, E. M., Yu, T., Campagnolo, F., Bottasso, C. L., Zanotti, A., and Croce, A.: Numerical and Experimental Study of Wake Redirection Techniques in a Boundary Layer Wind Tunnel, *J. Phys. Conf. Ser.*, 854, 012048, <https://doi.org/10.1088/1742-6596/854/1/012048>, 2017.
- Weckwerth, T. M. and Romatschke, U.: Where, When, and Why Did It Rain during PECAN?, *Mon. Weather Rev.*, 147, 3557–3573, <https://doi.org/10.1175/MWR-D-18-0458.1>, 2019.
- Weckwerth, T. M., Hanesiak, J., Wilson, J. W., Trier, S. B., Degelia, S. K., Gallus, W. A., Roberts, R. D., and Wang, X.: Nocturnal Convection Initiation during PECAN 2015, *B. Am. Meteorol. Soc.*, 100, 2223–2239, <https://doi.org/10.1175/BAMS-D-18-0299.1>, 2019.
- Welch, P.: The use of fast Fourier transform for the estimation of power spectra: a method based on time averaging over short, modified periodograms, *IEEE T. Acoust. Speech*, 15, 70–73, <https://doi.org/10.1109/TAU.1967.1161901>, 1967.
- Wharton, S.: `awaken/sa1.lidar.z01.00`, Wind Data Hub for U.S. Department of Energy, Office of Energy Efficiency and Renewable Energy [data set], <https://doi.org/10.21947/1915018> (last access: 1 July 2024), 2023.
- Wiersema, D. J., Lundquist, K. A., Mirocha, J. D., and Chow, F. K.: Evaluation of Turbulence and Dispersion in Multiscale Atmospheric Simulations over Complex Urban Terrain during the Joint Urban 2003 Field Campaign, *Mon. Weather Rev.*, 150, 3195–3209, <https://doi.org/10.1175/MWR-D-22-0056.1>, 2022.
- Wise, A. S.: Atmospheric boundary layer modeling for wind energy: assessing the impacts of complex terrain and thermally stratified turbulence on wind turbine performance, Ph.D. dissertation, University of California, Berkeley, 2024a.
- Wise, A. S.: Large-eddy simulation of an atmospheric bore and associated gravity wave effects on wind farm performance in the Southern Great Plains, Zenodo [video], <https://doi.org/10.5281/zenodo.12551369>, 2024b.
- Wise, A. S.: `adamwise95/WRFv4.4-DRM_GAD:WRFv4.4-DRM_GAD (v1.0)`, Zenodo [code], <https://doi.org/10.5281/zenodo.15492528>, 2025.
- Wise, A. S., Neher, J. M. T., Arthur, R. S., Mirocha, J. D., Lundquist, J. K., and Chow, F. K.: Meso- to microscale modeling of atmospheric stability effects on wind turbine wake behavior in complex terrain, *Wind Energ. Sci.*, 7, 367–386, <https://doi.org/10.5194/wes-7-367-2022>, 2022.
- Wong, V. C. and Lilly, D. K.: A comparison of two dynamic subgrid closure methods for turbulent thermal convection, *Phys. Fluids*, 6, 1016–1023, <https://doi.org/10.1063/1.868335>, 1994.

- Wyngaard, J. C.: Toward Numerical Modeling in the “Terra Incognita”, *J. Atmos. Sci.*, 61, 1816–1826, [https://doi.org/10.1175/1520-0469\(2004\)061<1816:TNMITT>2.0.CO;2](https://doi.org/10.1175/1520-0469(2004)061<1816:TNMITT>2.0.CO;2), 2004.
- Zhou, B. and Chow, F. K.: Large-Eddy Simulation of the Stable Boundary Layer with Explicit Filtering and Reconstruction Turbulence Modeling, *J. Atmos. Sci.*, 68, 2142–2155, <https://doi.org/10.1175/2011JAS3693.1>, 2011.
- Zhou, B. and Chow, F. K.: Turbulence Modeling for the Stable Atmospheric Boundary Layer and Implications for Wind Energy, Flow, Turbulence and Combustion, 88, 255–277, <https://doi.org/10.1007/s10494-011-9359-7>, 2012.
- Zhou, B. and Chow, F. K.: Nested Large-Eddy Simulations of the Intermittently Turbulent Stable Atmospheric Boundary Layer over Real Terrain, *J. Atmos. Sci.*, 71, 1021–1039, <https://doi.org/10.1175/JAS-D-13-0168.1>, 2014.